THESIS FOR THE DEGREE OF LICENTIATE OF ENGINEERING

Neutron spectroscopy studies of vibrational and diffusional dynamics in organometal halide and oxyhydride perovskites

Rasmus Lavén

Department of Chemistry and Chemical Engineering
CHALMERS UNIVERSITY OF TECHNOLOGY
Göteborg, Sweden 2021

Neutron spectroscopy studies of vibrational and diffusional dynamics in organometal halide and oxyhydride perovskites

Rasmus Lavén

© Rasmus Lavén, 2021

Licentiatuppsatser vid Institutionen för kemi och kemiteknik
Chalmers tekniska högskola.
Nr 2021:12

Department of Chemistry and Chemical Engineering
Chalmers University of Technology
SE-41296 Göteborg, Sweden

Printed by Chalmers Reproservice
Göteborg, Sweden 2021

Neutron spectroscopy studies of vibrational and diffusional dynamics in organometal halide and oxyhydride perovskites

Rasmus Lavén
Department of Chemistry and Chemical Engineering
Chalmers University of Technology

Abstract

This thesis deals with inelastic and quasielastic neutron scattering studies on the dynamical properties of the organometal halide perovskite system $MA_{1-x}FA_xPbI_3$ (MA = methylammonium; FA = formamidinium) and of the layered perovskite-type oxyhydride $SrVO_2H$. These materials systems are of high interest for their excellent photovoltaic performance ($MA_{1-x}FA_xPbI_3$) and hydride-ion conductivity ($SrVO_2H$) and concomitant promise for various technological devices; however, the local structure and dynamics underpinning these materials properties remain unclear.

With regards to the $MA_{1-x}FA_xPbI_3$ system, the studies focused on the nature of the organic cation dynamics. For the parent compound, $FAPbI_3$ (x = 1), the results showed that, in the cubic phase, the FA cations undergo nearly isotropic rotations whilst in the lower temperature tetragonal phases, the FA cation rotations are anisotropic and more complex. For the solid solutions, $MA_{1-x}FA_xPbI_3$ (x = 0.6, 0.9), it was found that the hydrogen-bonding interactions around the FA cations are strengthened in the MA-doped materials, which provides an atomistic understanding of the improved stability of the perovskite structure of $FAPbI_3$ with doping of MA.

For $SrVO_2H$, the studies focused on the dynamical properties of the hydride-ions, and the results unraveled the nature of both the diffusional and vibrational dynamics. It was found that the hydride-ion diffusion can be described in terms of a correlated vacancy-assisted diffusion mechanism in the *ab*-plane of the crystal structure, with an enhanced rate for backward jumps. Interestingly, the vibrational modes of the hydride-ions were found to be split due to the antiferromagnetism. Analysis of the neutron scattering data in combination with density functional theory calculations reveal unusually large spin-phonon coupling, which highlights the interesting couplings between magnetism and the hydrogen dynamics that occurs in $SrVO_2H$.

These new insights adds significantly to the current understanding of the dynamical properties in these materials and may be important for the development of materials with properties optimized towards their application in technological devices, such as solar cells, and energy storage and conversion devices.

Keywords: *Metal halide perovskites, oxyhydrides, perovskites, quasielastic neutron scattering, diffusion, inelastic neutron scattering, phonons, hydrogen dynamics.*

List of publications

This thesis is based on the following publications:

I Cation Dynamics and Structural Stabilization in Formamidinium Lead Iodide Perovskites
K. Druzbicki, R. Lavén, J. Armstrong, L. Malavasi, F. Fernandez-Alonso, and M. Karlsson
The Journal of Physical Chemistry Letters **12** 3503-3508 (2021)

II Rotational dynamics of organic cations in formamidinium lead iodide perovskites
R. Lavén, M.M. Koza, L. Malavasi, A. Perrichon, M. Appel, and M. Karlsson
In Manuscript

III Diffusional Dynamics of Hydride Ions in the Layered Oxyhydride $SrVO_2H$
R. Lavén, U. Häussermann, A. Perrichon, M.S. Andersson, M. Sannemo Targama, F. Demmel, and M. Karlsson
Chemistry of Materials **33** 2967-2975 (2021)

IV Vibrational properties of $SrVO_2H$ with large spin-phonon coupling
R. Lavén, P. Moraes, M. Sannemo Targama, M. Karlsson, A.A. Leitão, P. Barros, O. Vekilova, and U. Häussermann
In Manuscript

Additional publication not included in the thesis:

V Resonant enhancement of grazing incidence neutron scattering for the characterization of thin films
A. Perrichon, A. Devishvili, K. Komander, G.K Pálsson, A. Vorobiev, R. Lavén, M. Karlsson, and M. Wolff
Submitted

Contribution report

My contributions to the included papers:

I I contributed to the planning of the INS experiments and I was the main responsible for the experimental data collection and analysis of the experimental data. I was responsible for writing the experimental parts of the paper.

II I contributed to the planning of the QENS experiments and I was the main responsible for the data collection and analysis of the experimental data. I was the main responsible for writing the manuscript.

III I contributed to the planning of the QENS experiments and I was the main responsible for the data collection and analysis of the experimental data. I was the main responsible for writing the paper.

IV I contributed to the planning of the INS and IR experiments and was the main responsible for data collection and analysis of the experimental data. The manuscript was written jointly with the other authors.

Contents

List of abbreviations

DFT	Density functional theory
DOS	Density of states
FA	Formamidinium
GDOS	Generalized density of states
HOIP	Hybrid organic inorganic perovskite
ILL	Institut Laue-Langevin
INS	Inelastic neutron scattering
MA	Methylammonium
MHP	Metal halide perovskite
OHM	Organometal halide perovskite
QENS	Quasielastic neutron scattering
RT	Room temperature
TOF	Time-of-flight
XRD	X-ray diffraction

Chapter 1

Introduction

A fundamental understanding of the atomic and electronic structure and dynamics of solids lies at the heart of both physics and chemistry and is in addition crucial for technological development using different types of materials. For example, the development of much of the nowadays used electronics (computers, smartphones etc.) were initially dependent on the invention of the transistor and semiconductor technology, which was only made possible by a fundamental understanding of the electronic properties of semiconductors, as developed around the 1930s to 1950s [1]. Thus, the development of new materials with superior applicable properties for use in society and technology is in many cases ultimately dependent on elucidating the atomistic origin of the material properties, which in the end can lead to a rational design of new materials. This thesis is focused on increasing our fundamental understanding of two different classes of interesting, and technologically relevant, classes of materials, namely organometal halide perovskites and transition metal oxyhydrides. The aim of this thesis is to study and elucidate the dynamical properties (vibrational and diffusional dynamics) of these materials, which is believed to be responsible for several of the intriguing properties these materials display. Such properties include beneficial optical properties, and ionic conductivity, which both are of relevance for the development of new, and environmentally friendly, energy technologies.

With respect to organometal halide perovskites (OHPs), these materials are currently attracting a huge research interest because of their beneficial optoelectronic properties which can be advantageously used in solar cells and lightning devices [3]. In addition, they are relatively cheap (compared to other solar cell technologies), consisting only of earth-abundant elements, and are known to be easy to make, which increase their competitiveness towards other solar cell technologies even more [3]. These materials have been known for several decades [4, 5], but their exceptional

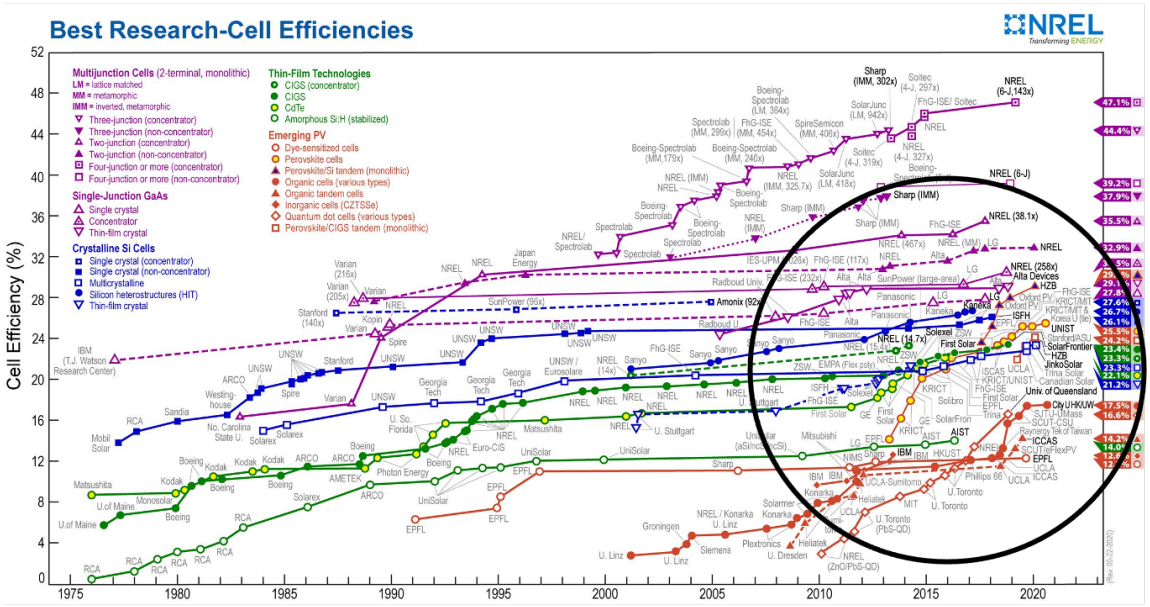

Figure 1.1: Illustration of the development of the power conversion efficiencies for solar cells based on various materials. The solar cells based on halide perovskites shown in yellow color and lies within the circled area. This plot is courtesy of the National Renewable Energy Laboratory, Golden, CO [2].

properties for energy conversion applications have only become apparent within the last ten years or so [6, 7], which has led to a huge amount of research being focused on OHPs. When used in a solar cell, the prototypical OHP methylammonium lead iodide ($MAPbI_3$) shows power conversion efficiencies around 20%, which is comparable to current Si based solar cells [3], see Figure 1.1. The main advantage of OHPs over conventional Si cells, is, however, the simplicity of their manufacturing and their high tolerance to internal defects [8]. While conventional Si cells require multi-step approaches under high temperature ($> 1000°$ C) and vacuum in cleanroom facilities [9], the OHPs can be synthesized using solution based methods in an ordinary chemistry lab [3]. Importantly, the OHPs can also be synthesized, with relatively ease, as a thin film using *e.g.* spin-coating or vapor deposition techniques [10], and because of the long carrier diffusion lengths in OHPs [11], the OHP can also function as a thin film solar cell device. As it turns out, however, the power conversion efficiency of solar cell devices made from OHPs have progressed more rapidly than the fundamental understanding of the physics and chemistry in these materials [8]. Structurally, the

metal halide perovskites are built from the perovskite structure with general chemical formula ABX_3 where A is an organic molecular cation (then they are called OHPs) (*e.g.* methylammonium, MA^+ or formamidinium, FA^+) or a large inorganic cation (*e.g.* Cs^+), B is a metal cation (*e.g.* Pb^{2+} or Sn^{2+}), and X is a halide anion (*e.g.* I^-, Br^-, or Cl^-). These materials display highly beneficial optoelectronic properties such as close-to-ideal bandgap for optimal photoabsorption from the solar spectrum, long diffusion lengths of the photo-excited electron and hole charge carriers, and low electron-hole recombination rates [12, 13]. Concerning a fundamental understanding of the OHPs, they exhibit certain phenomena that are not encountered in conventional inorganic semiconductors, such as Si, Ge or GaAs [8]. In particular, a specific feature of the OHPs is that the A-site molecular cation is dynamically disordered at non-cryogenic temperatures ($T \gtrsim 150$ K) [14], cf. Figure 1.2. Further, the lead halide perovskite framework is characteristic as "soft" or "floppy", *i.e.* it is composed of relatively large mass ions with weak ionic bonding leading to low phonon energies and intrinsic dynamic disorder [15–18]. These phenomena have been put forward for explaining several of the remarkable optoelectronic properties of OHPs [13]. For example, the large dynamical fluctuations, created from the organic cation dynamics and/or intrinsic dynamic disorder of the "soft" lead halide framework, have been argued to lead to large polaron formation and screening of charge carriers, leading to defect tolerance, moderate charge carrier mobility, and low recombination properties [18–21]. However, these phenomena are still not fully understood, and the proposed microscopic mechanisms lack in many cases direct experimental verification. The development of a full understanding of these intriguing properties requires systematic investigations of the temperature response of the lattice dynamics and the reorientational motions of the organic molecular cations in OHPs.

With respect to transition metal oxyhydrides, these are a very interesting class of materials in which the oxide anions in a transition metal oxide are partly replaced by hydride-ions to form the so-called oxyhydrides [23]. Transition metal oxides are in itself a very interesting class of materials with several interesting electronic phenomena such as magnetic, ferroelectric, superconductor, thermoelectric, and multiferroic properties, insulator-metal transitions, charge density waves, and mixed electronic/oxide-ion conduction [24]. The physical and chemical properties of transition metal oxides are typically tuned by cation substitution; thus, oxyhydrides allows to also modify the physical and chemical properties by modifications of the anion sublattice. Transition metal oxyhydrides have created an excitement for their magnetic [25, 26], catalytic [27], electronic [28] properties [29] and mixed ionic-electronic conductivity [30]. Especially the last mentioned property, hydride-ion conductivity, is particularly interesting, because it may allow for developing new solid state ionics

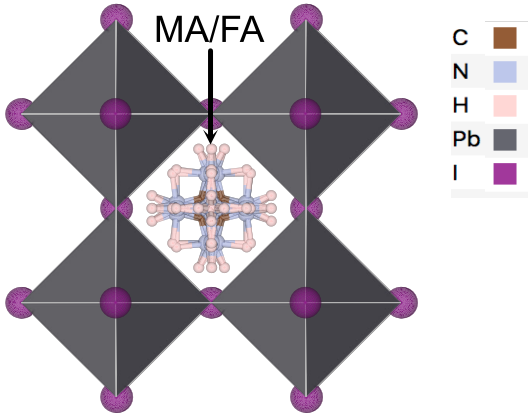

Figure 1.2: Crystal structure of an OHP with a dynamically disordered organic molecular cation on the A-site of the perovskite (right panel). The figure was generated using the VESTA software [22].

applications (fuel cells, batteries etc.) from oxyhydrides based on the conduction of hydride-ions. The hydride-ion conduction is made possible because the transition metal hydrogen bonding is relatively weak and creates an inherent lability for the hydride anion. For example, the hydride-ion mobility was already observed in 2006 in $LaSrCoO_3H_{0.7}$ by using neutron scattering techniques [31]. The lability of the hydride-ions was further corroborated for the case of $BaTiO_{3-x}H_x$ for which above 400 °C the exchange of H by D and N in the presence of D_2 and N_2, respectively, has been observed [32–34]. Recently Kobayashi *et al.* [35] demonstrated pure hydride-ion conductivity in $La_{2-x-y}Sr_{x+y}LiH_{1-x+y}O_{3-y}$, using a solid-state battery built from the oxyhydride. This created further excitement for the possibility of developing new and environmentally friendly energy technologies based on oxyhydrides. However, the hydride-ion diffusion mechanisms in oxyhydrides is far from being fully understood, and the development of new oxyhydride materials, with superior transport properties, is highly dependent on elucidating the mechanism of hydride-ion conductivity in these materials further.

With respect to these aforementioned open question regarding the dynamical properties of OHPs and oxyhydrides, neutron spectroscopy is a powerful experimental tool for directly probing the atomistic dynamics. Neutron spectroscopy is a powerful tool to investigate the nature of the dynamic response over a wide range of

energies and wavevectors, and allows to probe both the vibrational dynamics by inelastic neutron scattering (INS) and the diffusional dynamics by quasielastic neutron scattering (QENS). In this thesis, I have used INS and QENS in order to directly study the vibrational and diffusional dynamics in the OHP system $MA_{1-x}FA_xPbI_3$ and the oxyhydride $SrVO_2H$.

Chapter 2

Organometal halide perovskites

OHPs have attracted an enormous interest recently due to their promising applications as absorbers in photovoltaic devices. The prototypical OHPs that are of concern for this thesis are methylammonium lead iodide and formamidinium lead iodide ($MAPbI_3$, $MA = CH_3NH_3$, and $FAPbI_3$, $FA = CH(NH_2)_2$, respectively), which, when used in a solar cell, have shown power conversion efficiencies close to that of conventional Si solar cells [36, 37]. The main disadvantage of the perovskite solar cell is, however, its long-term stability towards humidity and heat [3]. Another concern about these materials is that the best performing materials contain lead, which is toxic. However, given the rapidly increasing amount of discovered metal halide perovskites with useful optoelectronic, and the large chemical space left to explore, there are most likely many more compounds waiting to be discovered, hopefully with higher stability, and without lead. A rational design of such materials is only possible when understanding how their atomistic structure and dynamics give rise to their beneficial optoelectronic properties.

2.1 Structural properties

Structurally, the OHPs are based on the versatile perovskite structure with general chemical formula ABX_3. The ideal structure is a cubic form ($Pm\overline{3}m$), which most metal halide perovskites display at sufficiently high temperature. However, this ideal cubic structure is rarely the ground state, and the perovskites generally display (one or several) phase transitions, upon lowering the temperature, to structures of lower symmetry. Fig 2.1 shows a typical phase behaviour of metal halide perovskites, *i.e.* a high temperature cubic phase, an intermediate temperature tetragonal phase, and a low temperature orthorhombic phase. However, the details of these phases

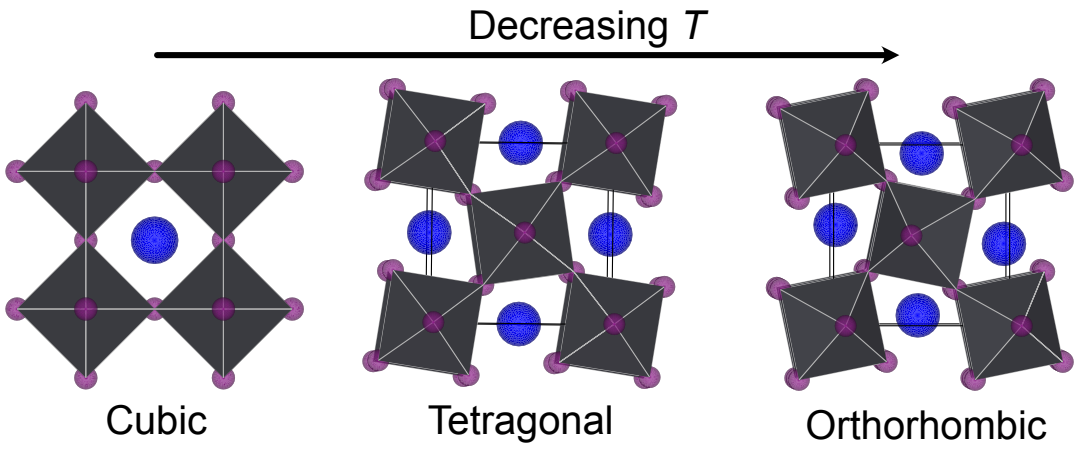

Figure 2.1: Illustration of cubic perovskite structure and typical phases of lower symmetry that often is formed at lower T. The A-site cation is illustrated as a blue sphere. The figure was generated using the VESTA software [22].

may differ depending on the A-site cation, and in what follows the structures of the two prototypical hybrid lead iodide perovskites $MAPbI_3$ and $FAPbI_3$, and their solid-solutions $MA_{1-x}FA_xPbI_3$, will be discussed.

2.1.1 Methylammonium lead iodide

The structure of $MAPbI_3$ is by now relatively well understood. In the early work by Poglitsch and Weber [5], it was established that $MAPbI_3$ shows three different crystal structures depending on temperature, *i.e.* a low-temperature orthorhombic phase ($T < 160$ K), a tetragonal phase $I4/mcm$ (160 K $< T <$ 330 K), and a high-temperature cubic phase $Pm\bar{3}m$ ($T > 330$ K). In the cubic phase, the MA cation was found to be dynamically disordered [5]. However, some structural details are still being debated [38], in particular with regard to the degree of ordering of MA and the space group assignment of the low-temperature structure. Poglitsch and Weber originally solved the orthorhombic low-temperature structure in the non-centrosymmetric space group $Pna2_1$ [5]. This was later refined to the centrosymmetric $Pnma$ space group by Baikie *et al.* [39], using single crystal X-ray diffraction (XRD). Weller *et al.* [40] provided a more complete structural picture, including MA orientations in tetragonal and orthorhombic phases, based on neutron powder diffraction data. In the tetragonal phase the MA cation was found to be disordered in the *ab*-plane along

four directions directed towards the faces of the distorted PbI_3 framework [40]. The orthorhombic structure could be solved in the *Pnma* space group, confirming the results by Baikie *et al.* [39]. In this *Pnma* structure, MA^+ cations are fully ordered in an antiferroelectric head-to-tail arrangement with the NH_3 pointing towards the distorted square face of the distorted perovskite structure [40]. However, a later study by Druzbicki *et al.* [41] have, by using INS combined with first-principles simulations, questioned the possibility of the *Pnma* structure to describe the INS data, which is particularly sensitive to the local environment around the MA cation. Even the commonly accepted centrosymmetric $I4/mcm$ model of the room-temperature (RT) phase has been recently questioned, based on the claim that the RT tetragonal phase of $MAPbI_3$ is ferroelectric [42]. The origin of ferroelectricity has been further clarified by Breternitz *et al.* [43] who refined the orthorhombic phase in the polar space group $I4cm$, by using single-crystal XRD. The detailed structure of the cubic phase has also recently been debated. Recent high-resolution X-ray total and inelastic scattering studies show that the cubic phase is made up of small dynamic tetragonal domains [44], however a recent INS study by Weadock *et al.* disproves this dynamic-domain hypothesis [45].

2.1.2 Formamidinium lead iodide

The stable phase of $FAPbI_3$ is a non-perovskite hexagonal structure at RT (yellow δ-phase $P6_3/mmc$) [46]. This phase has a too large electronic band gap for efficient solar absorption, and is thus of little relevance for photovoltaic applications [47, 48]. However, a cubic perovskite structure of $FAPbI_3$ (black α-phase, $Pm\overline{3}m$), with an optimal band gap for solar absorption (around 1.47 eV), can be stabilised at RT for about 10 days via heating above the hexagonal-to-cubic phase transition at 410 K [47–49].

Upon cooling the metastable cubic phase, a tetragonal phase (β-phase, $P4/mbm$) is formed below 285 K, and yet another structure is found below 140 K (γ-phase) [46, 50–53]. The structure of the low-temperature γ-phase is still not completely understood. Based on powder XRD data, Fabini *et al.* [51] refined the γ-phase in a new primitive tetragonal unit cell retaining the $P4/mbm$ symmetry, whilst Chen et al. [52] simultaneously refined neutron and X-ray diffraction patterns in a $1 \times 1 \times 6$ supercell ($P4bm$) of the intermediate tetragonal phase where the FA cation is rotated in increments around the *c*-axis. More recently, neutron powder diffraction experiments by Weber *et al.* [46] pointed towards a locally disordered γ-phase with possibly no long-range ordering of the FA^+ organic cations. The formation of an orientational glass of FA at low temperature has also been reported in previous

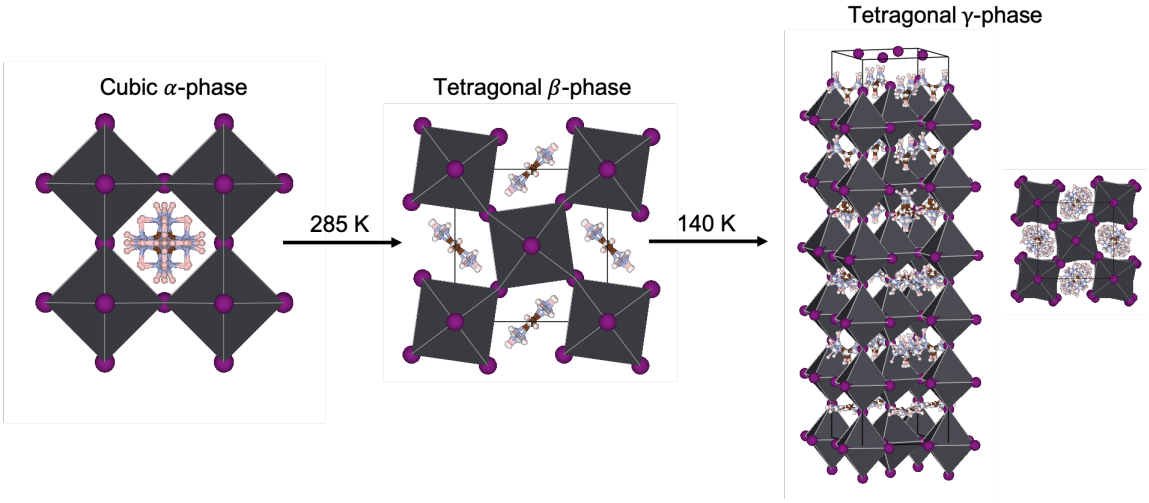

Figure 2.2: Illustration of the different crystal structures of $FAPbI_3$. Left panel: Cubic $FAPbI_3$. Note that in this phase the FA cation is disordered along all directions of the unit cell [50]. Mid panel: Intermediate tetragonal phase of $FAPbI_3$, as viewed along the c-axis, based on the model according to Weber *et al.* [46]. Right panel: Model of the low-temperature γ-phase according to Chen *et al.* [52]. This model is based on a $1 \times 1 \times 6$ expansion of the β-phase model where the FA cation is rotated in increments around the c-axis. I, C, N, and H atoms are depicted as purple, blue, brown, and pink spheres respectively. The Pb atoms lie within the black octahedra. The images were generated using the VESTA software [22].

thermodynamic property measurement [54] and local structure studies [55], which means that possibly the FA cation orientations are disordered in the γ-phase. The different structures of $FAPbI_3$ are illustrated in Fig. 2.2.

2.1.3 $MA_{1-x}FA_xPbI_3$ solid solutions

Due to the previously mentioned phase stability problem of $FAPbI_3$, a lot of efforts have recently been focused on the mixed-cation system $MA_{1-x}FA_xPbI_3$, which have been shown to stabilize the cubic perovskite structure of $FAPbI_3$ at RT, even for relatively low concentrations of MA [47, 56]. In addition, these mixed-cation systems show a higher stability towards humidity and heat than pure $MAPbI_3$, and are among the materials with highest power-conversion efficiencies when used in a perovskite photovoltaic device [3, 37, 57, 58]. The phase behaviour of $MA_{1-x}FA_xPbI_3$

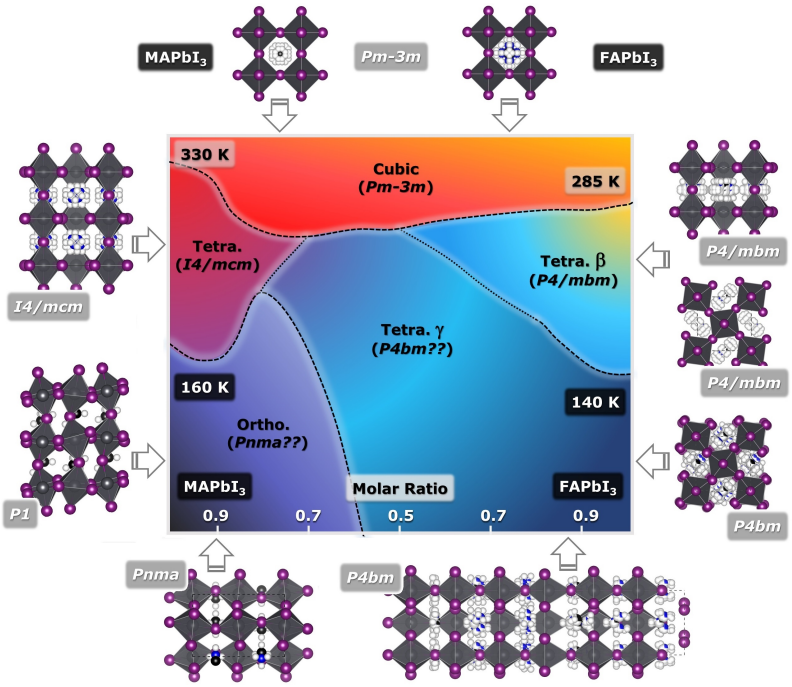

Figure 2.3: Illustration of the structural phase behaviour of the solid solutions $MA_{1-x}FA_xPbI_3$ according to Francisco Lopez *et al.* [59]. Pure $MAPbI_3$ and $FAPbI_3$ corresponds to the left and right edges of the diagram, respectively. Space group assignments that are still not completely solved are marked with question marks. Reprinted with permission from Ref. [38], Copyright (2021) American Chemical Society.

solid solutions have been recently studied by Francisco Lopez *et al.* [59], by Raman scattering and photoluminescence spectroscopy. The phase diagram as a function of temperature and x for the $MA_{1-x}FA_xPbI_3$ system is shown in Figure 2.3. The main results are that for low concentrations of FA, the phase behaviour is similar to that of $MAPbI_3$, while for FA concentrations above ca. 0.7, the phase behaviour is similar to that of $FAPbI_3$. Noticeably, for molar ratios of MA to FA close to 0.5, the intermediate temperature phase is completely suppressed, and the phase transition from cubic to the disordered low-temperature γ-phase occurs directly [59]. Summing up, these previous studies have clearly illustrated the difficulty in obtaining a complete understanding of the structural properties of OHPs. This is especially apparent when comparing results from different methods, for example crystallographic (diffraction)

results versus results from techniques more sensitive to the local or instantaneous structure; or when comparing X-ray and neutron scattering data. While for X-rays, the light elements present in the organic cations are virtually invisible, but they have large neutron cross section. Thus, X-ray scattering studies mainly "see" the lead halide framework, whilst neutron scattering studies are very sensitive to the organic cations. One can further note that the complexity created by the additional rotational degrees of freedom of the organic cations, and the intrinsic dynamic disorder of the lead halide framework, in these materials adds a further difficulty for a complete understanding of their structure.

While the atomic structure of a material is critical for understanding its properties, many materials properties are inherently linked to the atomistic dynamics. This is in particular true for systems like $MA_{1-x}FA_xPbI_3$ which are highly dynamical at ambient temperature. While $MA_{1-x}FA_xPbI_3$ has previously mainly been studied by crystallographic techniques, which yield the time-averaged structure, spectroscopic techniques, such as INS, is sensitive to correlation functions in both space and time, and can therefore provide additional information on the local structure and dynamics of the organic cations [38].

2.2 Dynamical properties

The dynamical properties of the organic cation in OHPs were realized already from the beginning. In the original work by Poglitsch and Weber in 1987 [5], millimeter-wave spectroscopy was used to observe dynamical relaxation on the picosecond timescale in $MAPbX_3$ (X = I, Br, and Cl), and which was interpreted in terms of dynamic disorder of the MA cations. Later on, after realizing the remarkable optoelectronic properties of OHPs, an emerging important question is the impact of the organic cation dynamics on the materials optoelectronic properties. This question has generated a lot of scientific interest over the past years [14, 55, 60–72], and still to date an understanding of the effect of the organic cation dynamics remains elusive. The organic cation dynamics (in particular that of MA which have an electric dipole) have, however, been invoked for explaining several of the material properties, such as, for example, microscopic ferroelectric domains [60], lowering of the exciton binding energy [14], hot carrier cooling [73], and charge recombination rates [19, 74, 75]. Specifically, both experimental and theoretical studies have suggested that the dynamic disorder created by the rotation of the dipolar molecular cation creates potential fluctuations which can lead to an increased separation of the charge carriers, which, consequently, leads to reduced recombination rates [74, 75]. This was further established by Chen *et al.* [52] who measured the recombination

rates in all crystallographic phases of $MAPbI_3$ and $FAPbI_3$ and found that phases with higher rotational entropy give rise to longer carrier lifetimes. However, a recent study also showed that the dynamical potential fluctuations also are present for the all-inorganic material $CsPbBr_3$ and might thus be intrinsic to the inorganic sublattice [18]. Notably, OHPs have been claimed to belong to the class of materials known as "phonon glass electron crystals", meaning that they show 'band-like' charge carrier dynamics and "glass-like" phonons [20, 21]. It has further been argued that this "crystal-liquid duality" is responsible for large electron polaron formation and screening of charge carriers, leading to defect tolerance, moderate charge carrier mobility, and low radiative recombination properties [19–21]. This behaviour has been argued to be an effect of the weak ionic bonding and relatively large atomic masses of the lead halide frameworks [18] and the organic molecular cation reorientational motions [20]. However, a complete understanding of the nature and effect of the organic cation and perovskite lattice dynamics on the structural and optical properties of MHPs remains in many ways elusive.

A particularly suitable technique for probing the organic cation dynamics in OHPs is neutron spectroscopy. This is because their dynamics occurs at time and length scales directly accessible to neutron scattering [5, 14], and the large incoherent neutron cross section of hydrogen, which is present in the organic cation ends, make neutrons particularly sensitive to the organic cation dynamics. The localized rotational motions of the organic cations have been directly probed in previous studies by QENS for the MA-containing compounds $MAPbI_3$ [14, 60, 61, 65], $MAPbBr_3$ [66, 76], and $MAPbCl_3$ [77, 78]. As a primary example, Chen *et al.* [14] used a group theoretical symmetry analysis of their QENS data to show that for $MAPbI_3$, in the RT tetragonal structure and high temperature cubic phase, the whole MA cation performs rotations of four-fold symmetry around the crystallographic c-axis, whilst in the low-temperature orthorhombic phase, only the three-fold rotations of the methyl and/or ammonia group around the C−N axis persist (See Figure 2.4 for an illustration of these motions). They could further correlate their results for the MA rotational dynamics to the low exciton binding energy and low charge recombination rate in $MAPbI_3$. Interestingly, the onset of cation reorientations in the tetragonal phase of $MAPbI_3$ was found to correlate with a giant increase in the dielectric function. As the exciton binding energy is inversely proportional to the dielectric function, which determines the strength of the Coulomb interaction between charges in a material, this suggests that cation reorientations is responsible for lowering the exciton binding energy in this material [14]. Contrastingly, the cation dynamics in $FAPbI_3$ have been studied much less than for $MAPbI_3$. A QENS study on $FAPbBr_3$ was recently reported by Sharma *et al.* [79]. They showed that

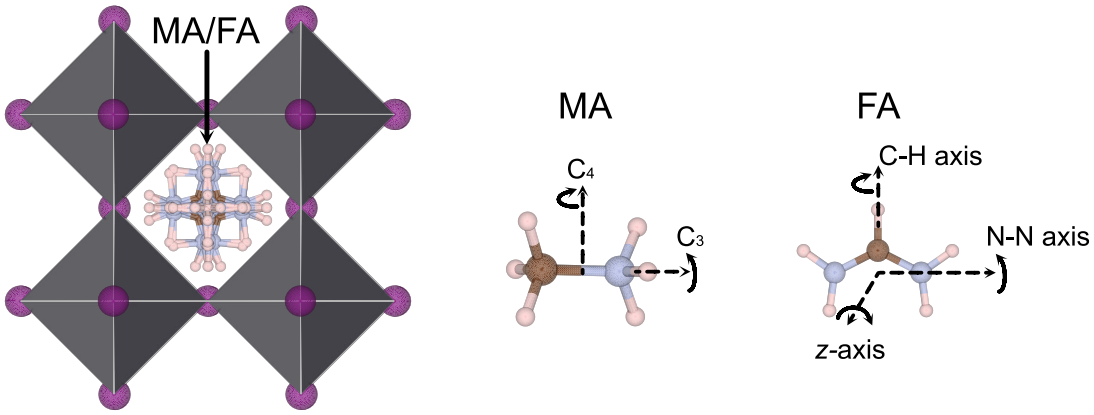

Figure 2.4: Schematic illustration of the cubic crystal structure of OHPs with a dynamically disordered organic cation at the A-site of the perovskite. The various possible rotational modes of MA and FA are illustrated [13]. The images were generated using the VESTA software [22].

the FA cation performs isotropic rotations for all measured temperatures ($100 - 350$ K) with an increasing fraction of FA cations contributing to the dynamics with increasing temperature. However, Mozur *et al.* [80, 81] have found that that the FA cation orientation and dynamics in $FAPbBr_3$ relates to unusual temperature trends in the photoconductivity and that the dynamics is highly dependent on local structural distortions. The FA cation dynamics in $FAPbI_3$ have also been investigated by several experimental techniques [55, 62, 82, 83]. For example, Fabini *et al.* [55] used a combination of nuclear magnetic resonance, dielectric spectroscopy, and molecular dynamics simulations to show that the FA cation primary reorients along the N...N axis (see Figure 2.4) in all crystallographic phases, with a relaxation time of about 8 ps at RT. In another study by Kubicki *et al.* [62] it was found using nuclear magnetic resonance (NMR) that at RT the FA cation rotation in $FAPbI_3$ is more than one order of magnitude faster than for MA in $MAPbI_3$, despite the larger size of FA. These results are at variance with the NMR results reported by Fabini *et al.* who showed that the reorientation rate of MA and FA in $MAPbI_3$ and $FAPbI_3$ are very similar at RT [55]. Thus, a complete understanding of the FA cation dynamics in $FAPbI_3$ is still lacking. However, with the increasing interest in the mixed FA/MA systems, more information of the organic cation dynamics, in particular of the FA cation, is needed.

Chapter 3

Transition metal oxyhydrides

3.1 Structure and properties

Transition metal oxyhydrides are a relatively small but steadily growing family of mixed anion compounds which are based on the anions O^{2-} and H^-. One of the earliest reported transition metal oxyhydrides was discovered by Hayward *et al.* in 2002 [23]. They reported the synthesis of $LaSrCoO_3H_{0.7}$ upon reduction with CaH_2 of the Ruddlesden-Popper phase oxide precursor $LaSrCoO_4$. This material generated a lot of scientific interest, mainly because of the possible novel electronic and magnetic properties that could be introduced with the hydride-ions. In addition, questions were raised concerning the mechanism of hydride-ion insertion into the oxide, and $LaSrCoO_3H_{0.7}$ was subsequently investigated with respect to magnetic and electronic properties [84] and hydride-ion diffusion [31].

This relatively simple synthesis method developed by Hayward and coworkers [23], 'topochemical' reaction with CaH_2 (or other metal hydrides), also provided more opportunities for further discoveries of novel oxyhydride phases upon hydride reduction of transition metal oxides. However, the number of discovered transition metal oxyhydrides is still relatively small to date. This is because whilst the topochemical reduction of transition metal oxides with metal hydrides can often be performed to form highly reduced oxide phases, with unusual transition metal coordination environment, hydride insertion is still relatively rare [85, 86]. In 2012, Kobayashi *et al.* reported the synthesis of $BaTiO_{3-x}H_x$ (with x up to 0.6) [32], which shortly after was followed to include the series $ATiO_{3-x}H_x$ (A = Ba, Sr, and Ti) [30, 87]. This was the first example of an oxyhydride based on the simple cubic perovskite structure. Later on, other perovskite-type oxyhydrides, such as $SrVO_2H$ [89] and $SrCrO_2H$ [88] have been reported. Even though the cubic perovskite structure is regarded as relative

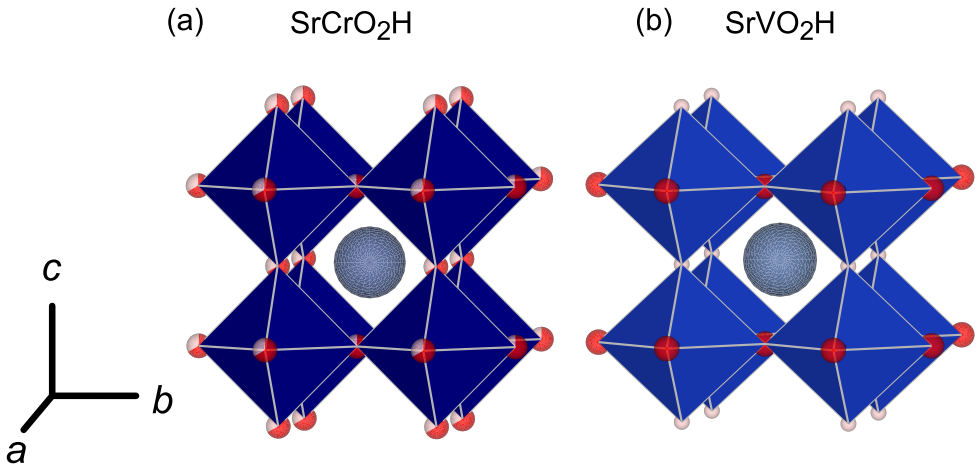

Figure 3.1: (a) Crystal structure of cubic $SrCrO_2H$ according to Ref. [88]. Sr, O, and H atoms are shown as grey, red, and pink spheres respectively. The Cr ions are inside the dark blue octahedra. The 2/3 red and 1/3 pinked colored spheres illustrates the disorder between H and O. (b) Crystal structure of anion-ordered tetragonal $SrVO_2H$ according to Ref. [89]. The images were generated using the VESTA software [22].

simple, depending on the kind of transition metal and hydride-ion concentration and distribution, different scenarios have been encountered. The structural diversity of perovskite-type transition metal oxyhydrides is clearly illustrated by the fact that both $ATiO_{3-x}H_x$ (A = Ba, Sr) [32, 87] and $SrCrO_2H$ [88] display an average cubic perovskite structure in which the O^{2-} and H^- anions show a perfect solid solution behavior [Figure 3.1 (a)]. A strikingly different scenario is encountered for $SrVO_2H$, which has the same stoichiometry as $SrCrO_2H$, where the O^{2-} and H^- anions are perfectly ordered in a tetragonal structure, that is related to the cubic perovskite structure [89], see Figure 3.1 (b). $BaTiO_{3-x}H_x$, with Ti in a mixed IV/III oxidation state, is paramagnetic (above the lowest temperature measured of 5 K) [32]. Both $SrCrO_2H$, with Cr^{3+} d^3 species, and $SrVO_2H$, with V^{3+} d^2 species (Figure 3.2), are antiferromagnets where the magnetic ordering is intact above RT. The Néel temperature of $SrCrO_2H$ is 380 K [88] and > 400 K for $SrVO_2H$ [89, 90]. For both $SrCrO_2H$ and $SrVO_2H$, the antiferromagnetic (AFM) structure is of G-type with a 10-atom body-centered tetragonal unit cell, that is based of a $\sqrt{2} \times \sqrt{2} \times 2$ exansion of the non-magnetic cell [88, 89]. The AFM structure of $SrVO_2H$ is shown in Figure 3.2(a).

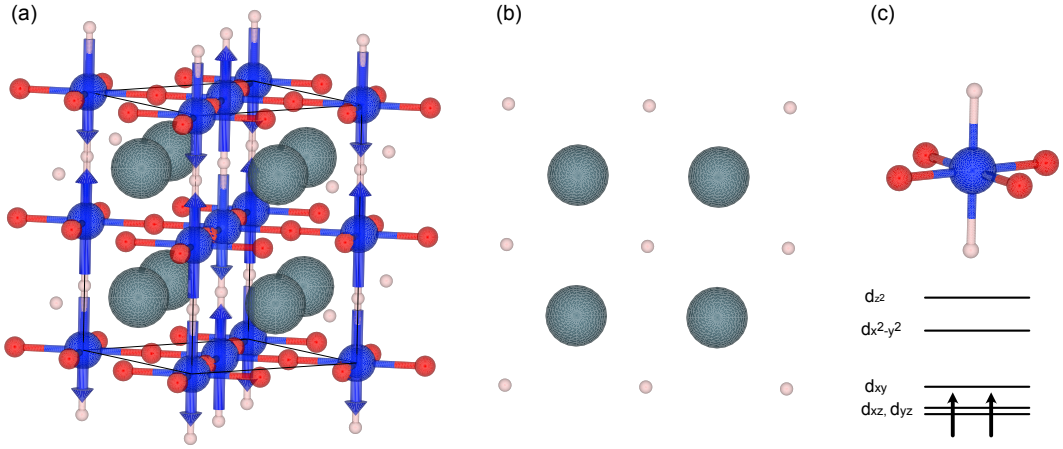

Figure 3.2: Schematic illustrations of the structure of $SrVO_2H$. (a) Illustration of the antiferromagnetic structure of $SrVO_2H$ according to Ref. [89]. Sr, V, O, and H ions are shown as grey, blue, red, and pink spheres, respectively. The antiferromagnetically ordered spins of the V^{3+} cations lie parallel to the *c*-axis. (b) Illustration of the *ab*-plane of the crystal structure where the hydride-ions lie coordinated to Sr in a square-planar fashion. (c) Local coordination of V by 4 O and 2 H leads to a $(d_{xz}, d_{yz})^2$ electronic state [89]. The images were generated using the VESTA software [22].

Transition metal oxyhydrides show a variety of interesting and useful properties, including electron transport, mixed ionic-electronic conductivity, magnetic, and catalytic properties [29]. $SrVO_2H$, for example, has generated a lot of interesting for its interesting electronic and magnetic properties. $SrVO_2H$ has thus been investigated theoretically with respect to electronic and magnetic properties, finding unusual strong magnetic couplings that are dependent on the hydride-ions [25, 26]. Further, a pressure dependent XRD study has shown that the hydride-ions in $SrVO_2H$ are extraordinarily compressible, and that pressure drives an insulator-to-metal transitions [28].

In general, transition metal oxyhydrides allow for interesting magnetic and electronic properties to occur, because it may allow to access unusual low oxidation states of the transition metals. Such materials include, for example, the recently discovered 4*d* transition metal oxyhydrides $LaSr_3NiRuO_4H_4$ and $LaSrCo_{0.5}Rh_{0.5}O_3H$ [91, 92] and $LaSrMnO_{3.3}H_{0.7}$ [93] that can be stabilized by high pressure methods.

3.2 Hydride ion dynamics

The initial study of hydride-ion dynamics in transition metal oxyhydrides was reported in 2006 by Bridges *et al.* [31] by QENS. The QENS data showed the presence of hydride-ion diffusion for temperatures above 675 K, which is close to the decomposition temperature of the sample material. Analysis of the QENS data showed that the diffusion mechanism could be interpreted in terms of vacancy-assisted hydride-ion jump diffusion along the a-axis in the crystal structure. The hydride-ion diffusion was only observed for temperatures near or above the sample decomposition temperature, and in conjunction with hydrogen loss, whereas below 675 K no hydride-ion diffusion was observed on the probed timescales [31]. Later on, the lability of the hydride-ions was once more demonstrated, for the case of the perovskite oxyhydride $BaTiO_{3-x}H_x$, for which above 400 °C the exchange of H by D and N in the presence of D_2 and N_2, respectively, was observed [32–34]. This demonstrated that the hydride-ions are mobile in $BaTiO_{3-x}H_x$ and thus raised questions about possible hydride ion diffusion mechanisms. Following these works, the hydride-ion diffusion in $ATiO_{3-x}H_x$ (A = Ba and Sr) has been studied with several different experimental and computational techniques [94–98]. Tang *et al.* [95] reported gaseous hydrogen release/exchange experiments and first-principles simulations which were interpreted in terms of a hydride-ion diffusion mechanism that is highly dependent on the concentration of hydride ions (x), with the simultaneous movement of oxygen ions for $x < 0.4$, whereas for $x > 0.4$ only the hydride ions diffuse. The activation energy was found to significantly decrease with increasing x until around $x = 0.4$ after which it was roughly constant. The activation energy for for both of these processes were, however, found to be relatively high, in the range of 3.85–2 eV [95]. However, in another computational study, a much lower activation energy of about 0.28 eV was reported for oxygen-vacancy mediated hydride-ion diffusion [96]. The hydride-ion diffusion in $SrTiO_{3-x}H_x$ was also studied using isotope exchange and depth profiling methods combined with density functional theory calculations by Liu *et al.* [98]. The results indicated a highly correlated long-range transport of hydride-ions that is impeded by slow reorganization of the oxygen sublattice. The hydride-ion dynamics in $BaTiO_{3-x}H_x$ samples characterized by a relatively large concentration of oxygen vacancies, was further studied using QENS by Eklöf-Österberg *et al.* [97]. The QENS data showed the presence of a highly temperature dependent diffusion mechanism, characterized by hydride-ion jumps between nearest neighbour oxygen vacancies below 250 K, and with the presence of hydride-ion jumps between next-nearest neighbouring oxygen vacancies at higher temperatures (T >400 K).

The recent study by Kobayashi *et al.* [35], which demonstrated pure hydride-ion

conductivity in $La_{2-x-y}Sr_{x+y}LiH_{1-x+y}O_{3-y}$[1], using a solid-state battery built from the oxyhydride, have created further excitement with the aim of developing new solid state ionics applications based on H^- conduction using oxyhydride materials [99]. However, the hydride-ion diffusion mechanisms in oxyhydrides is far from being fully understood, and the development of new oxyhydride materials, with superior properties, is highly dependent on elucidating the mechanism of hydride-ion conductivity further. A primary tool for this purpose is neutron scattering, which will be described in the following chapter.

[1]Note that this material does not contain any transition metal elements, and might therefore not be considered as a *transition metal* oxyhydride.

Chapter 4

Neutron scattering

4.1 Basic considerations

4.1.1 General characteristics of neutron scattering

This section gives a brief overview of neutron scattering as an experimental technique used in the condensed matter sciences, and follow mainly the references [100–102]. The scattering of cold and thermal neutrons[1] is an important experimental tool with applications over a wide range of science including physics, chemistry, and biology. The usefulness of neutrons to probe condensed matter stem from the fundamental properties of the neutron [100]. Firstly, the neutron have no electric charge and, consequently, interact directly with the nuclei of the sample material, via nuclear interactions. This means that the neutron can penetrate deep into the sample, ensuring that bulk properties are being probed. In addition, the nuclear interaction varies randomly over the periodic table, and allows also for isotope contrast. Of specific concern to this thesis, hydrogen has a very large scattering cross section by neutrons and thus scatter neutrons very strongly, whilst it is virtually invisible to X-rays. Secondly, the de Broglie wavelength of thermal neutrons is of the order of interatomic spacings in solids. Consequently, neutron diffraction measurements can be performed to obtain information on the atomic structure [100]. Thirdly, the energies of thermal and cold neutrons are on the order of $1-100$ meV, which is of the

[1]Thermal neutrons refer to neutrons with energies around $10-100$ meV, which is similar to the thermal energy at RT ($k_{\mathrm{B}}\,T \approx 25$ meV). Cold neutrons refer to neutrons having energies lower than this, around $0.1-10$ meV. The term temperature is used because the neutrons produced in a reactor or spallation neutron source are moderated in a medium with a certain temperature. The energy distribution of the moderated neutrons will then be a Maxwell-Boltzmann distribution with a maximum at $3k_{\mathrm{B}}\,T/2$ with T being the moderator temperature [102]

same order as the energies of many excitations in solids, such as phonons, magnons (and other magnetic excitations), and crystal field excitations. The measurements of inelastically scattered neutrons thus allow to probe such excitations. Lastly, the neutron has a magnetic moment, which means that it can interact with unpaired electrons in magnetic solids. This makes neutron scattering sensitive also to magnetic structures, and magnetic excitations [100].

4.1.2 Theoretical description of the scattering process

The measured quantity in a neutron scattering experiment is related to differential cross section $\mathrm{d}^2\sigma/\mathrm{d}\Omega\mathrm{d}E_\mathrm{f}$, which is proportional to the number of neutrons scattered per second into a small solid angle $\mathrm{d}\Omega$ and with final energy between E_f and $E_f+\mathrm{d}E_\mathrm{f}$. This scattering process is illustrated in Figure 4.1 (a). For a theoretical understanding of the scattering process, consider a neutron characterized by a plane wave with initial wavevector $\mathbf{k}_i$ and energy $E_i = \hbar^2 k_i^2/2m$ incident on a sample, which is scattered *via* the nuclear interaction with the sample into another state with a final wavevector $\mathbf{k}_f$ and energy $E_f = \hbar^2 k_f^2/2m$. m is here the neutron mass and $\hbar$ is the reduced Planck constant. The scattering data is typically expressed in terms of the wavevector transfer[2] $\mathbf{q}$ and the energy transfer E, defined as, $\mathbf{q} = \mathbf{k}_i - \mathbf{k}_f$, and $E = E_i - E_f$. From, this one sees that $\mathbf{q}$ and E are not independent variables because the neutron energy depends on its wavevector. The magnitude of the wavevector transfer $q = |\mathbf{q}|$, can be expressed as

$$q^2 = |\mathbf{k}_i - \mathbf{k}_f|^2 = k_i^2 + k_f^2 - 2\,k_i\,k_f\,\cos\theta = \frac{2m}{\hbar^2}\left(E_i + E_f - 2\sqrt{E_i E_f}\cos\theta\right), \quad (4.1)$$

where θ is the angle between the incident and final neutron wavevectors (See Figure 4.1 (a)). From this equation its clear that (q, E) region that can be probed in an experiment is limited and that it depends on the incident neutron energy, and the largest scattering angle θ that can be measured. In particular, this will lead to a curved region in (q, E)-space being measured in an experiment. This is illustrated in Figure 4.1 (b) which shows the INS data collected from a powder sample of $MAPbI_3$. Note that the probed region in (q, E) space is not a rectangle, but curved.

The interaction between the nuclei in the scattering system and the neutron is of short-range, several orders of magnitude shorter than the neutron wavelength. The neutron-nucleus interaction can thus be approximated by the so-called Fermi

[2]The momentum transfer is $\hbar\mathbf{q}$; thus, q is commonly also referred to as the momentum transfer.

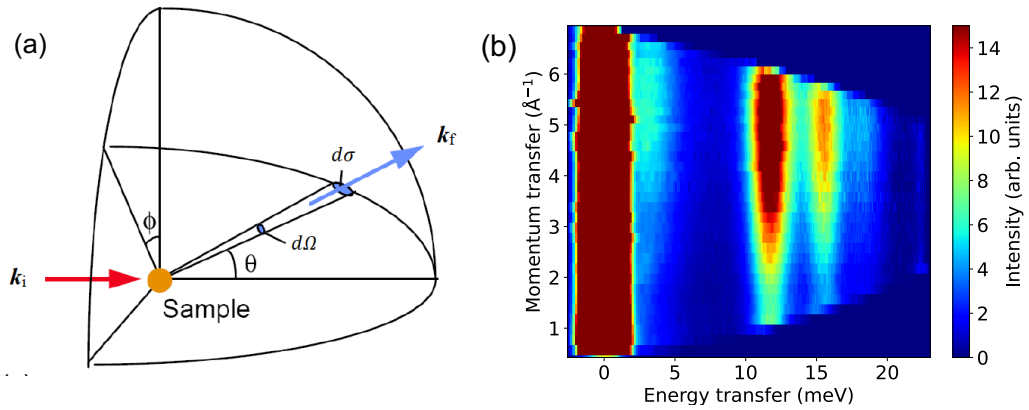

Figure 4.1: (a) Illustration of the scattering geometry in a neutron scattering experiment in real space. Adapted from [100, 103]. (b) INS data of a powder sample of $MAPbI_3$ at 2 K. The data were obtained from the IN5 spectrometer at the Instut Laue-Langevin using an incident neutron wavelength of 1.7 Å.

pseudopotential [100]

$$V(\mathbf{r}) = \frac{2\pi\hbar^2}{m} \sum_j b_j \delta(\mathbf{r} - \mathbf{R}_j),$$

where b_j is the so-called neutron scattering length of nucleus j and $\mathbf{R}_j$ is the position vector of nucleus j. The neutron-nucleus interaction can therefore be characterized by a single parameter, the scattering length b. b varies randomly with the atomic mass number, and depends on the spin state of the neutron-nucleus system. The integrated total cross section of such a potential is $\sigma_{\text{tot}} = 4\pi b^2$, which can be interpreted as an "effective area" of the nuclei which the neutron "sees". An expression for the double differential cross section $\mathrm{d}^2\sigma/\mathrm{d}\Omega\mathrm{d}E_\mathrm{f}$ can be written as [100]

$$\frac{\mathrm{d}^2\sigma}{\mathrm{d}\Omega\mathrm{d}E_\mathrm{f}} = \frac{k_f}{k_i}\frac{1}{2\pi\hbar}\sum_{j,j'} b_j b_{j'} \int_{-\infty}^{\infty} \mathrm{d}t \left\langle \exp\left(-\mathrm{i}\mathbf{q}\cdot\mathbf{R}_{j'}(t=0)\right)\exp\left(\mathrm{i}\mathbf{q}\cdot\mathbf{R}_j(t)\right)\right\rangle \times \exp\left(-\mathrm{i}E\,t/\hbar\right), \tag{4.2}$$

where $\mathbf{R}_j(t)$ is the time-dependent position operator of nuclei j in the Heisenberg picture, and the brackets $\langle \ldots \rangle$ refer to the thermal average[3]. Note that b_j is here the

[3]For an operator A the thermal average is given by $\langle A\rangle = \sum_\lambda p_\lambda \langle\lambda|A|\lambda\rangle$, where

$$p_\lambda = \frac{\exp(-E_\lambda/k_\mathrm{B}T)}{\sum_\lambda \exp(-E_\lambda/k_\mathrm{B}T)}$$

scattering length of nuclei j which may vary randomly from one nucleus to another because of different nuclear spin states and/or the presence of isotopes. By letting f_i be the relative frequency of the value b_i, the average value of the scattering length can be written as $\overline{b} = \sum_i f_i b_i$. Assuming no correlation between the scattering lengths of different nuclei, one may write [100]

$$\overline{b_{j'} b_j} = (\overline{b})^2, \qquad j' \neq j, \tag{4.3}$$

$$\overline{b_{j'} b_j} = \overline{b^2}, \qquad j' = j. \tag{4.4}$$

By taking the average of the different possible distributions of b_j values in Eq. (4.2), it can conventionally be rewritten in terms of coherent and incoherent neutron scattering as

$$\frac{\mathrm{d}^2\sigma}{\mathrm{d}\Omega \mathrm{d}E_\mathrm{f}} = \left(\frac{\mathrm{d}^2\sigma}{\mathrm{d}\Omega \mathrm{d}E_\mathrm{f}}\right)_\mathrm{coh} + \left(\frac{\mathrm{d}^2\sigma}{\mathrm{d}\Omega \mathrm{d}E_\mathrm{f}}\right)_\mathrm{inc}, \tag{4.5}$$

where the coherent and incoherent parts are respectively given by the expressions [100]:

$$\left(\frac{\mathrm{d}^2\sigma}{\mathrm{d}\Omega \mathrm{d}E_\mathrm{f}}\right)_\mathrm{coh} = \frac{\sigma_\mathrm{coh}}{4\pi}\frac{k_f}{k_i}\frac{1}{2\pi\hbar}\sum_{j,j'}\int_{-\infty}^{\infty}\mathrm{d}t\,\langle \exp\left(-\mathrm{i}\mathbf{q}\cdot\mathbf{R}_{j'}(t=0)\right)\exp\left(\mathrm{i}\mathbf{q}\cdot\mathbf{R}_j(t)\right)\rangle$$
$$\times \exp\left(-\mathrm{i}E\,t/\hbar\right), \text{ and} \tag{4.6}$$

$$\left(\frac{\mathrm{d}^2\sigma}{\mathrm{d}\Omega \mathrm{d}E_\mathrm{f}}\right)_\mathrm{inc} = \frac{\sigma_\mathrm{inc}}{4\pi}\frac{k_f}{k_i}\frac{1}{2\pi\hbar}\sum_{j}\int_{-\infty}^{\infty}\mathrm{d}t\,\langle \exp(-\mathrm{i}\mathbf{q}\cdot\mathbf{R}_j(t=0))\exp(\mathrm{i}\mathbf{q}\cdot\mathbf{R}_j(t))\rangle$$
$$\times \exp\left(-\mathrm{i}E\,t/\hbar\right). \tag{4.7}$$

Here, $\sigma_\mathrm{coh} := 4\pi(\overline{b})^2$ and $\sigma_\mathrm{inc} := 4\pi(\overline{b^2} - (\overline{b})^2)$ are the so-called coherent and incoherent cross sections, respectively. It can be seen that the coherent scattering depends on the correlation of the same and different nucleus at different times. The coherent scattering thus contains interference effects of the scattered neutrons (including diffraction). The incoherent scattering, on the other hand, depends only on the correlations of the same nuclei at different times, and does not therefore contain any interference effects. The incoherent scattering arises due to the random deviations of the scattering lengths from their mean value, for each type of nucleus in the sample [100]. It should be noted that even for the incoherent neutron scattering, there is always a coherent superposition of the outgoing neutron waves − it is only the

is the probability that the scattering system is in the state λ [100].

averaging process that leads to a cancellation of the phase factors [102]. Thus, the coherent scattering is the scattering which the same system would give if all scattering lengths were given by the mean value $\bar{b}$, whilst the incoherent scattering is the term one must add to obtain the scattering from the actual system [100]. This separation of the scattering cross section into a coherent and an incoherent part is especially useful for samples containing H, because the incoherent cross section of H is 80.26 barn whilst the coherent part is only 1.75 barn [102].[4] Thus, neutron scattering by hydrogen is largely dominated by the self-terms, and the measured scattering signal can in most cases be interpreted in terms of self-dynamics. For neutron diffraction experiments, however, samples containing H can sometimes be problematic because the incoherent scattering gives a large background in the diffraction data. Thus, it is common in diffraction experiments to replace H by deuterium (D), because D possess the twin advantage of having a much smaller σ_{inc} and a larger σ_{coh}. However, for QENS and INS studies, where one probes dynamics, and which is of specific concern in this thesis, it is beneficial to have a large incoherent cross section. It should be pointed out that, even though this separation of coherent and incoherent terms is useful for many isotopes where one of these terms are considerably larger than the other it may still be complicated to interpret for isotopes were the incoherent and coherent cross sections are similar. That is, one probes the sum of the coherent and incoherent scattering, where the coherent contains both self and cross terms, whilst the incoherent contains the self terms only [102].

The double differential cross section can conveniently be expressed in the following form,

$$\frac{\mathrm{d}^2\sigma}{\mathrm{d}\Omega \mathrm{d}E_{\mathrm{f}}} = \frac{k_f}{4\pi k_i}\left[\sigma_{\text{coh}} S_{\text{coh}}(\mathbf{q}, E) + \sigma_{\text{inc}} S_{\text{inc}}(\mathbf{q}, E)\right], \tag{4.8}$$

where $S_{\text{coh}}(\mathbf{q}, E)$ and $S_{\text{inc}}(\mathbf{q}, E)$, are the so-called coherent and incoherent dynamical structure factors, respectively. As it turns out, the dynamical structure factors are very useful quantities, and are what is normally derived from a neutron scattering measurement. Further, the incoherent and coherent dynamical structure factors, are the Fourier transforms in space and time of the self and pair correlation functions $G_{\text{s}}(\mathbf{r}, t)$ and $G(\mathbf{r}, t)$, respectively [104]. Consequently, the coherent and incoherent scattering gives respectively information about correlations between different nuclei at different times, and on self correlations.

[4] 1 barn $= 1 \times 10^{-24}$ cm^2.

4.2 Inelastic neutron scattering

Inelastic scattering refers to events where the neutron exchanges energy with the scattering system. The neutron can both create and annihilate excitations with energy E, leading to neutron energy loss and gain, respectively[5]. Clearly, the scattering by annihilation of excitations is heavily dependent on their population, *i.e.* on temperature. The neutrons can scatter of phonons by nuclear interaction or magnetic excitations via magnetic interactions. In this thesis only nuclear scattering will be considered. Further, neutrons can interact with particles performing stochastic motions (diffusion or rotation), leading to so-called *quasielastic scattering*, as will be discussed in detail in section 4.3. A schematic sketch of the elastic, quasielastic, and inelastic scattering components as can be measured in a neutron scattering experiment, is illustrated in Figure 4.2. The inelastic peaks occur at non-zero energy transfer values and, in the case of phonon scattering, they occur at energy transfer values corresponding to the energy of the vibrational motion. Thus INS can be used to study the vibrational dynamics of materials. A particular advantage of INS over the commonly applied Raman and infrared spectroscopies, is that no optical selection rules apply; thus, in principle, all modes are measurable [105] (though their intensity depend on the neutron scattering cross section). In addition, neutron scattering allows to probe a wide range of wavevectors, and can give access to the (neutron cross section-weighted) vibrational density of states. Below, I will discuss the neutron scattering of phonons (or vibrational motions) in more detail.

4.2.1 Phonon scattering

In this thesis, all studied materials contain a relatively large amount of H. Because of the large incoherent cross section of H, the coherent scattering can then be neglected, *i.e.* $S(q,E) \approx S_{\mathrm{inc}}(q,E)$. For incoherent scattering by one phonon, it can be shown that the expression for the double differential cross section can be written in terms of the phonon density of states $g(\omega)$ as [106]

$$\left(\frac{\mathrm{d}^2\sigma}{\mathrm{d}\Omega \mathrm{d}E_{\mathrm{f}}}\right)_{\mathrm{inc}} = \frac{\sigma_{\mathrm{inc}}}{4\pi}\frac{1}{12M}\frac{k_f}{k_i}e^{-2W}q^2\frac{g(\omega)}{\omega}\left[\coth\left(\frac{\hbar\omega}{2k_{\mathrm{B}}T}\right)\pm 1\right], \tag{4.9}$$

where M is the mass of the vibrating atom, $\omega = E/\hbar$, e^{-2W} is the so-called Debye-Waller factor, and the factor $\coth(\hbar\omega/2k_{\mathrm{B}}T)\pm 1$ stands for the Bose-Einstein population factor for phonon creation and annihilation, respectively. Thus, for a given q,

[5] In Raman spectroscopy, this is commonly referred to as Stokes and anti-Stokes scattering, respectively.

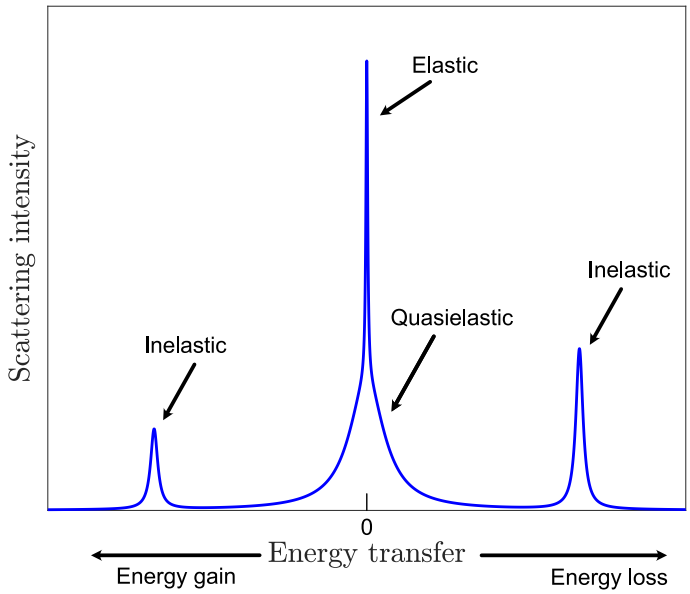

Figure 4.2: Schematic sketch of the elastic, quasielastic, and inelastic scattering components in a neutron scattering experiment. The quasielastic scattering refers to the broadening of the elastic peak, which occurs at $E = 0$. The inelastic peaks occur at non-zero energy transfer values. The intensities of the inelastic peak at the neutron energy gain side depends heavily on temperature. At low temperature, only inelastic scattering on the neutron energy loss side can be observed because there is no population of the excitations.

all modes whose energy satisfy $\hbar\omega = E$ contribute to the scattering. The 1-phonon incoherent scattering is thus proportional to the phonon density of states and can be used to derive a so-called generalized density of states (GDOS) from the experiment. The GDOS, $G(\omega)$, is a weighted sum and can be written as [106]

$$G(\omega) = \sum_i \frac{\sigma_{\text{inc}}^{(i)}}{4\pi} \frac{1}{M_i} e^{-2W_i} g_i(\omega), \tag{4.10}$$

where the index i refers to the properties of atom i in the unit cell, and the sum runs over all atoms in the unit cell. The difference between the GDOS and the real phonon density of states, is that the different atomic contributions in the GDOS is weighted by σ_i/m_i where σ_i and M_i are the scattering cross section and mass, respectively, of atom i [107]. Figure 4.3 shows the GDOS extracted from incoherent neutron scattering of a powder sample of $MAPbI_3$ at $T = 100$ K. Note that because of the

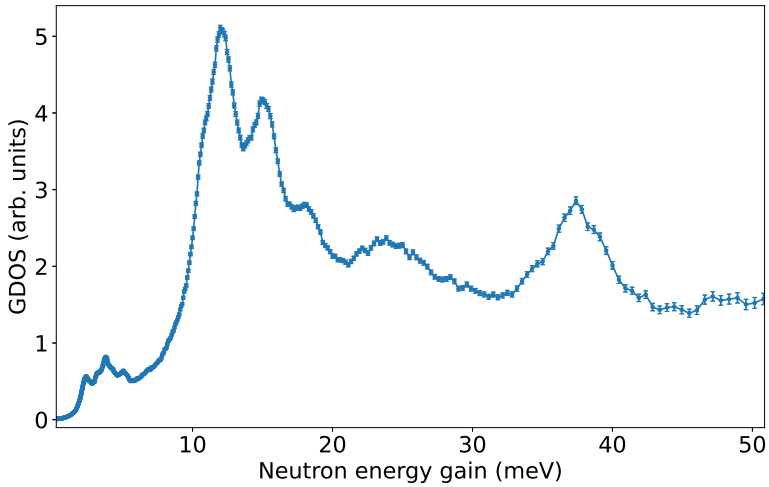

Figure 4.3: GDOS as extracted from neutron time-of-flight data obtained at IN5 at the ILL, of a powder sample of $MAPbI_3$ at $T = 100$ K.

large incoherent scattering cross section of H, and the low mass of the MA organic cation compared to Pb and I, the GDOS will be dominated by vibrations related to the organic cation. The GDOS is featured by several sharp peaks corresponding to the molecular librations of the MA organic cation in $MAPbI_3$ [38, 41].

4.3 Quasielastic neutron scattering

Quasielastic neutron scattering (QENS) refers to the broadening of the elastic line which occurs due to interactions between the neutrons and atoms in the sample performing translational and/or reorientational diffusional dynamics on the timescale $\hbar/\Delta E$, where ΔE is the energy broadening [102, 108]. As it turns out, QENS is most easily understood in terms of correlation functions in space and time and this description is originally due to Van-Hove [104]. In this thesis, all studied materials contain H, and because of the large incoherent cross-section of H, the quasielastic coherent scattering can be safely neglected. Thus, only the incoherent quasielastic scattering is considered in what follows. As we saw above, the incoherent neutron scattering is determined by the incoherent dynamical structure factor $S_{\text{inc}}(\mathbf{q}, E)$, which is the Fourier transform in both space and time of the self-correlation function $G_s(\mathbf{r}, t)$. $[G_s(\mathbf{r}, t)\,\mathrm{d}^3 r]$ gives the probability that, given a particle at the origin at

$t = 0$, the same particle is in the volume d^3r at position $\mathbf{r}$ and at time t [102]. The Fourier transform in space of $G_s(\mathbf{r}, t)$ yields the self-part of the so-called intermediate scattering function $I_s(\mathbf{q}, t)$, and the Fourier transform of $I_s(\mathbf{q}, t)$ in time yields the dynamical structure factor $S_{\text{inc}}(\mathbf{q}, E)$ which is what is commonly[6] obtained in a (incoherent) QENS experiment.

A useful characteristic of QENS is that it is possible to separate the cases of long-range (translational) and localized (restricted) diffusion. For localized diffusion, there is a finite probability that the particle will be at the original position at $t \to \infty$. This will lead to that the $I_s(q, t)$ has a non-zero value at $t = \infty$. In turn, after Fourier transform, this leads to a separate elastic component for $S_{\text{inc}}(\mathbf{q}, E)$. The typical behaviour for $S_{\text{inc}}(\mathbf{q}, E)$ and $I_s(q, t)$ for localized and long-range diffusional motions is schematically illustrated in Figure 4.4, and these two cases will be discussed separately in what follows.

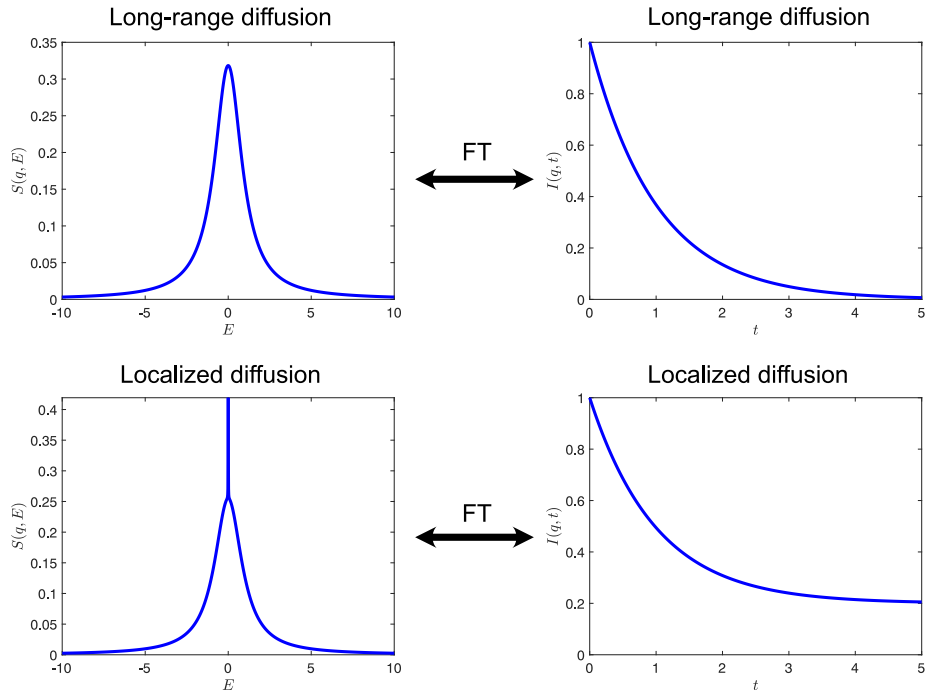

Figure 4.4: Schematic illustrations of the incoherent $S(q, E)$ and the self-part of $I(q, t)$ for long-range and localized (restricted) diffusion. The $I(q.t)$ and $S(q, E)$ are related by a Fourier transform (FT).

[6]In neutron spin-echo spectroscopy, one measures the intermediate scattering function $I(\mathbf{q}, t)$, rather than $S(\mathbf{q}, E)$.

4.3.1 Long-range translational diffusion

In the macroscopic limit (large distances, corresponding to a small q in reciprocal space), the self-correlation function obeys the standard diffusion equation $\partial_t G_s(r,t) = D\nabla^2 G_s(r,t)$, with the initial condition $G(r, t=0) = \delta(r)$ and where D is the (self) diffusion coefficient [102]. The solution to this equation can be written as [102]

$$G_s(r,t) = \frac{1}{(4\pi D\,|t|)^{3/2}} \exp(-r^2/4D|t|).$$

The Fourier transform of this function yields the following $I_s(q,t)$ and $S_{\text{inc}}(q,E)$:

$$I_s(q,t) = \exp(-q^2 D|t|) \tag{4.11}$$

$$S_{\text{inc}}(q,E) = \frac{1}{\pi}\frac{\hbar D q^2}{(\hbar D q^2)^2 + E^2}. \tag{4.12}$$

Thus, $S_{\text{inc}}(q,E)$ is a single Lorentzian function with linewidth (HWHM) $\hbar D q^2$. This law is generally true for small q, but for larger q the details of the diffusion mechanism becomes important. In particular, for jump diffusion in solids, the linewidth at higher q must mimic the jump rate, as will be explained below.

A common model for diffusion on a lattice is the Chudley-Elliot model which considers jump diffusion in a Bravais lattice where the particle stays a mean residence time τ on a site before an instantaneous jump to a nearest neighbouring site. The results for $I_s(q,t)$ and $S_{\text{inc}}(\mathbf{q},E)$ are the following [102, 109]

$$I_s(\mathbf{q},t) = \exp\left[-\frac{t}{N\tau}\sum_j^N (1 - e^{-i\mathbf{q}\cdot\ell_j})\right] \tag{4.13}$$

$$S_{\text{inc}}(q,E) = \frac{1}{\pi}\frac{\gamma(\mathbf{q})}{\gamma(\mathbf{q})^2 + E^2}. \tag{4.14}$$

The linewidth $\gamma(\mathbf{q})$ is in this case given by,

$$\gamma(\mathbf{q}) = \frac{\hbar}{N\tau}\sum_{j=1}^{N}\left[1 - e^{-i\mathbf{q}\cdot\ell_j}\right], \tag{4.15}$$

where the sum runs over all nearest neighbour sites ℓ_j with N being the number of nearest neighbours. For small q, Eq. (4.15) gives the macroscopic limit $\gamma \to \hbar D q^2$. Whilst for larger q, γ approaches the jump rate, $\gamma \to \hbar/\tau$. For studies of polycrystalline samples, no information of the direction of $\mathbf{q}$ can be obtained, and

it is then common to approximate the powder averaged scattering signal by using an isotropic average over all directions of $\gamma(\mathbf{q})$. The jump length is then assumed identical for all sited and thus becomes an "effective" quantity d. The isotropically averaged linewidth then becomes [102, 109]

$$\gamma(q) = \frac{\hbar}{\tau}[1 - j_0(q\,d)], \tag{4.16}$$

where $j_0(x) = sin(x)/x$ is the zeroth-order spherical Bessel function. Still it should be noted that this is only approximately correct and, in principle, the powder average should be performed over the whole $S_{\mathrm{inc}}(\mathbf{q}, E)$ [102].

4.3.2 Localized diffusion

Localized diffusion can also be studied using QENS. This can for example be localized rotational/reorientational motions of molecules or molecular groups in solid phases as is studied in Paper II of this thesis. For localized (or confined) diffusion, there is a finite probability that the particle is present at the original position when $t \to \infty$. This means that $I_s(q,t)$ will not decay to zero, but to a finite value, for $t \to \infty$. After the Fourier transform, this yields an intrinsic elastic component in $S_{\mathrm{inc}}(q, E)$, see Figure 4.4. The relative intensity of this elastic component is commonly referred to as the elastic incoherent structure factor (EISF), and the q-dependence of the EISF can be used to gain information of the spatial geometry of the localized dynamics. The EISF is the limit of $I_s(q,t)$ as $t \to \infty$ and can be calculated as [102]

$$\mathrm{EISF} = \frac{1}{N^2}\left|\sum_j e^{\mathbf{iq}\cdot\mathbf{r}_j}\right|^2, \tag{4.17}$$

where $\mathbf{r}_j$ $j = 1, \ldots N$ is the sites the particle can visit. Consequently, the EISF for jump rotation over any arrangement of discrete sites can be calculated [102, 108]. For powder samples, the results obtained from Eq. (4.17) has to be spatially averaged over all directions.

Experimentally, the EISF can be estimated by determining the ratio of elastic to elastic plus quasielastic scattering intensity *i.e*

$$\mathrm{EISF} = \frac{I_{\mathrm{el}}}{I_{\mathrm{el}} + I_{\mathrm{qe}}},$$

where I_{el} and I_{qe} is the elastic and quasielastic scattering intensity, respectively. A common, "model-free", approach for determining the geometry of localized motions

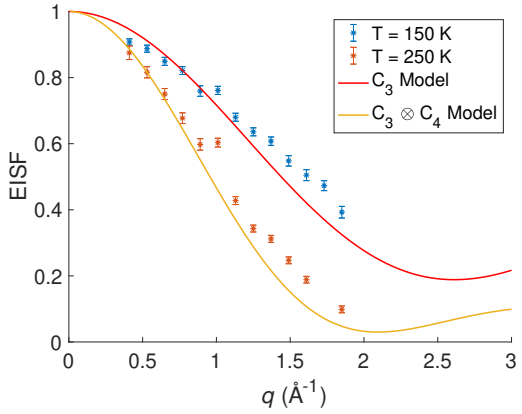

Figure 4.5: EISF of $MAPbI_3$ at 150 K and 250 K from QENS data obtained on the IN6 spectrometer at the ILL [Paper II].

by QENS, is thus to fit the QENS data a model function of the following form

$$S(q,E) \propto \left[I_{\mathrm{el}}\,\delta(E) + \sum_i I_{\mathrm{qe}}^{(i)}\,\mathcal{L}(E;\gamma_i) \right] \circledast R(q,E) + \mathrm{bkg}(q,E), \tag{4.18}$$

where the delta function describes the elastic peak with intensity I_{el} and where one or several Lorentzian functions $\mathcal{L}(E;\gamma_i)$ with linewidth (HWHM) γ_i describes the quasielastic scattering, with total intensity $I_{\mathrm{qe}} = \sum_i I_{\mathrm{qe}}^{(i)}$. $\mathrm{bkg}(q,E)$ is background function, that usually is described as a linear function of energy. The elastic and quasielastic parts are convoluted by the function $R(q,E)$ which describes the instrument resolution function. The fraction of elastic scattering can then be derived as a function of q, which then can be compared to different jump diffusion models describing localized diffusion. An example of this approach is shown in Figure 4.5, which shows the EISF of $MAPbI_3$ extracted from QENS fitting at 150 K and 250 K. The data is compared to two different models. The C_3 model describes three-fold rotation of the methyl and ammonia groups around the C−N axis. The $C_3 \otimes C_4$ describes a combined C_3 rotation of the methyl/ammonia groups and a four-fold rotation of the whole MA molecule, as was described by Chen *et al.* [14]. As can be seen, the data in the orthorhombic phase at 150 K is in good agreement with the C_3 model. The data at 250 K, however, shows smaller EISF (larger portion of quasielastic scattering), than what the C_3 model predicts, and is in good agreement with the $C_3 \otimes C_4$ model (see paper II for details).

Chapter 5

Experimental methods

There are several different types of neutron spectrometers, utilizing different technical approaches for measuring the scattered neutrons as a function of energy and momentum transfer. In this thesis, I have used two different experimental techniques for INS, namely neutron time-of-flight spectroscopy, and neutron backscattering spectroscopy. The main characteristic difference between these two techniques is that they probe different parts of (q, E) space, with different resolutions. Since the measured scattering signal is related to the Fourier transform of correlation functions in real space and time, different parts of the probed momentum and energy space translates into different probed length- and time-scales, respectively, of the dynamics in the studied systems. The probed timescale can roughly be related to the energy transfer by $\sim \hbar/E$, and the probed length scale can roughly be related to the momentum transfer by $\sim 2\pi/q$. More specifically, neutron backscattering spectroscopy, allows to achieve the highest possible energy resolution (in the μeV range), thus allowing to probe slow timescale dynamics, on the order of nanoseconds. However, for neutron backscattering the energy transfer window is quite limited and in order to access larger energy transfers (*i.e.* faster timescale dynamics), neutron time-of-flight spectroscopy has been used. In what follows, I will describe the basics of neutron time-of-flight and backscattering spectroscopy.

5.1 Neutron time-of-flight spectroscopy

A common technique for inelastic neutron scattering is neutron time-of-flight spectroscopy. As examples, both IN5 and IN6 at the Institut Laue-Langevin (ILL) located in Grenoble, France, which were used in this thesis, are time-of-flight (TOF) spectrometers. The basic idea in TOF spectroscopy is that the neutron energy is

measured by measuring the time it takes for the neutron to cover a well-defined distance between the sample and a detector. If the time and distance are known, the neutron velocity can be determined, and the velocity can be related to the corresponding neutron energy.

There are two types of TOF spectrometers, called direct geometry spectrometers and indirect geometry spectrometers. In a direct geometry spectrometer, the incident energy is fixed, whilst for an indirect geometry spectrometer, the final neutron energy is fixed. For simplicity, we only here consider a direct geometry spectrometer, which is the most simple technical setup to understand.

In a direct geometry spectrometer, the beam has first to be monochromatized and pulsed (in order to set the incident 'time' of the neutrons). This can be done in several ways. For example, on the TOF spectrometer IN6 at the ILL, diffraction of a well-known single-crystal is used for monochromatizing the beam which is then pulsed by using series of rotating disks, called choppers. The choppers are rotating disk made from neutron absorbing material, with transparent slits that allows to create a pulsed beam. Another method is used on the TOF spectrometer IN5 at the ILL, where the beam is both monochromatized and pulsed using disk choppers. After the beam has been pulsed and monochromatized, the time it takes for the neutron to reach the detector can then be used to measure its energy. The wavevector of the scattered neutron is measured by having detectors at different positions, which are translated into various scattering angles. An illustration of the TOF spectrometer IN5, which can be considered as a prototypical direct-geometry TOF spectrometer, is shown in Figure 5.1

The recorded raw data in a TOF experiment, $N(2\theta, \mathrm{TOF})$, thus contains the number of counted neutrons as a function of their TOF and scattering angle 2θ (Figure 5.2). It is therefore necessary to reduce the raw data and apply different corrections in order to obtain the wanted dynamical structure factor $S(q, E)$, which, ideally, is method-independent *i.e.* only contain information of the sample. In this thesis, this was done in the following steps. Since the number of counts depend on the measurement time, it was normalized to the monitor count. The efficiency of the detectors were accounted for by normalizing to measurements on a vanadium sample. V is (approximately) a purely incoherent scatterer, $\sigma_{\mathrm{coh}} \approx 0.0184$ barn and $\sigma_{\mathrm{inc}} \approx 5.08$ barn, and the scattering of V is thus roughly isotropic. This normalization is done by integrating the vanadium measurement over time-of-flight channels around the elastic peak and then divide by this for each detector, i.e.

$$N(2\theta, \mathrm{TOF}) \rightarrow \frac{N(2\theta, \mathrm{TOF})}{\int_{\text{elastic peak}} d\mathrm{TOF}\ N_{\mathrm{Vanadium}}(2\theta, \mathrm{TOF})}.$$

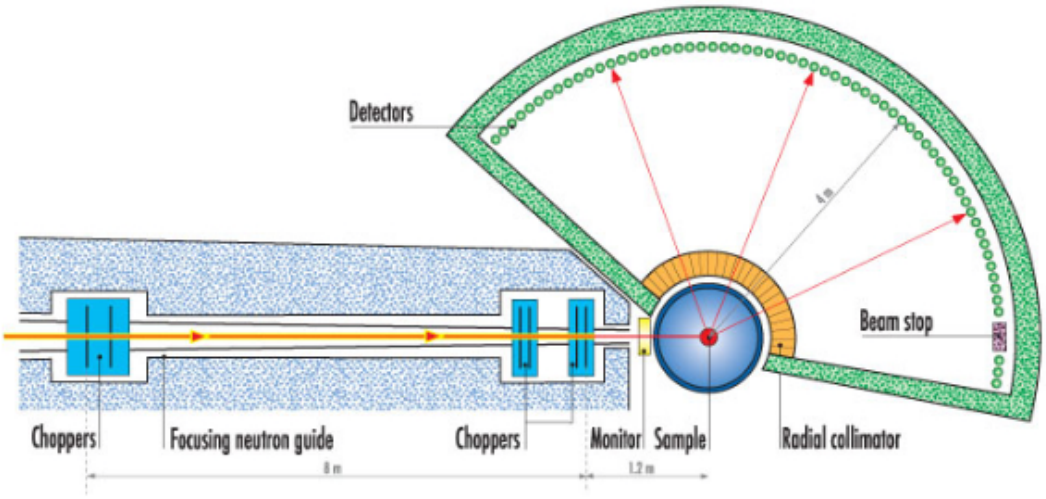

Figure 5.1: Schematic sketch of the direct-geometry time-of-flight spectrometer IN5 at the ILL, Grenoble, France. The figure was taken from [110].

Measurements on an empty cell should be subtracted in order to remove the scattering from the sample holder and cryostat (or possible from other parts of the instrument). The empty can measurements need also before this subtraction to be normalized to monitor count and a vanadium standard. The neutron detectors efficiency also depends on the neutron energy, and needs to be corrected for. For this purpose, for the cases of IN6 and IN5, special empirical relations can be used that are implemented in the data analysis software LAMP [111]. The result is then related to the double differential cross section $d^2\sigma/d\Omega d\mathrm{TOF}$ (number of neutrons per time scattered into the solid angle $d\Omega$ and with time-of-flight in the range $d\mathrm{TOF} + \mathrm{TOF}$). This is still measured as a function of the time-of-flight and scattering angle, and needs to be converted to the (q, E) domain. The wave vector transfer q is related to the scattering angle and energy transfer according to

$$q^2 = |\mathbf{k}_i - \mathbf{k}_f|^2 = k_i^2 + k_f^2 - 2\,k_i\,k_f\,\cos\theta = \frac{2m}{\hbar^2}\left(E_i + E_f - 2\sqrt{E_i E_f}\cos\theta\right). \quad (5.1)$$

Hence, q depends on both the scattering angle and the energy transfer non-linearly. Therefore one scattering angle does not corresponds to one q, but it changes with energy transfer. The TOF instrument thus probes a curved region of the (q, E) space. Figure 5.3 shows an illustration of the data reduction steps in TOF spectroscopy. Note that once converted to the (q, E) domain, the probed domain is

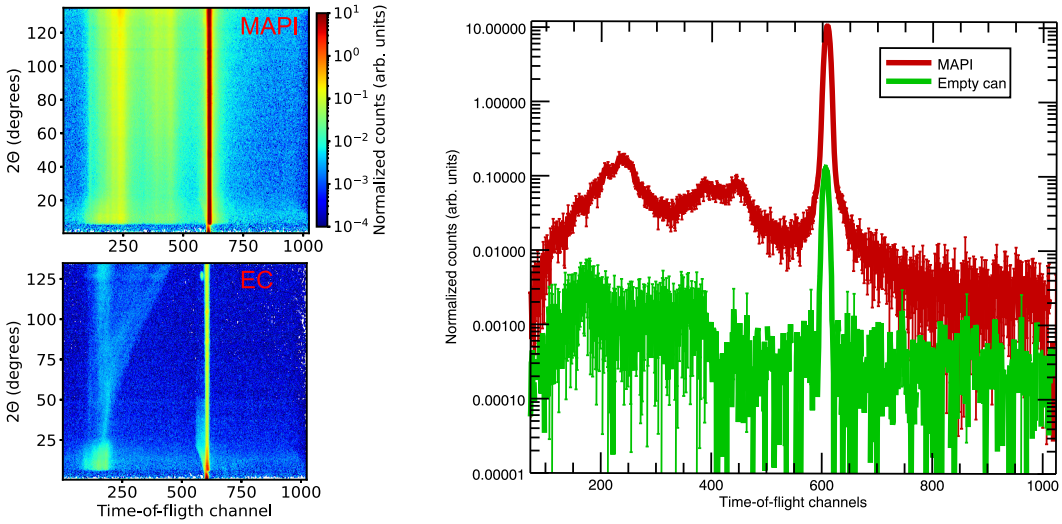

Figure 5.2: Raw time-of-flight data from IN5 on $MAPbI_3$ and the empty sample can (EC) at $T = 100$ K showing the scattering data as a function of scattering angle and time-of-flight channel (time). The right panel shows the time-of-flight spectra for $2\theta = 115°$.

curved. The maximum energy loss is roughly 2 meV in this case of 5 Å incident wavelength neutrons and is determined by the incident neutron energy (the neutron cannot lose more energy than it has). The maximum energy gain is, in principle, unlimited; though it is limited by the time between neutron pulses, so that the fastest neutrons do not overlap with the slowest neutrons in the previous pulse; in Figure 5.3 it is only shown up to -50 meV after conversion to $S(q, E)$. After this treatment, the measured dynamical structure factor $S(q, E)$ is still convoluted with the instrumental resolution function $R(q, E)$. For the purpose of QENS analysis, this can be determined by measurements of the sample at low temperature (2 K) where all dynamics is assumed to be frozen-in (no quasielastic scattering), or by measurements of a vanadium sample, which scatters only elastically. Further corrections of the data that were not mentioned here might include multiple scattering corrections, and corrections for absorption and self-shielding of the sample.

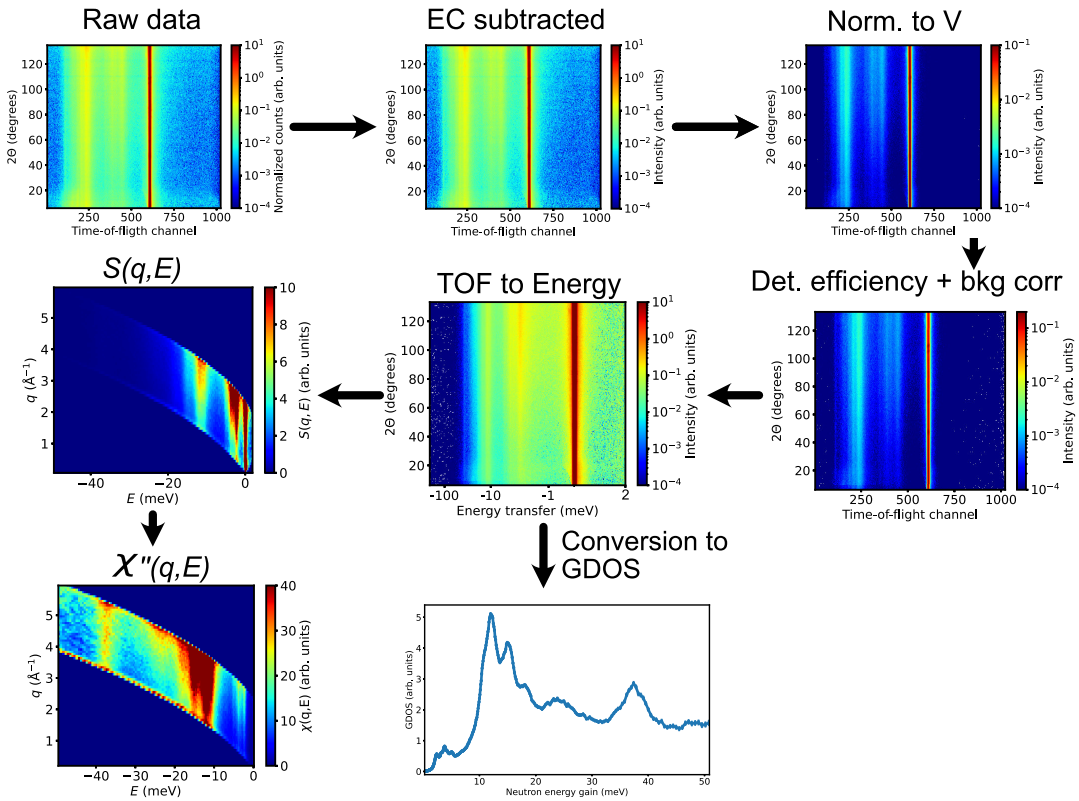

Figure 5.3: Illustration of some data reduction steps for conversion from the raw neutron TOF data to the measured dynamical structure factor $S(q, E)$, the GDOS, or the dynamic susceptibility $\chi''(q, E)$ which is related to the dynamical structure factor by a correction for the Bose population *i.e.* $S(q, E) = (1/\pi)[1+n(E)]\chi''(q, E)$, where $n(E) = [\exp(E/k_bT) - 1]^{-1}$ denotes the Bose-Einstein population factor. The plot of $\chi''(q, E)$ shows the absolute value of $\chi''(q, E)$ which otherwise is an odd function of energy. The TOF data was taken on a powder sample of $MAPbI_3$ at 100 K using an incident neutron wavelength of 5 Å. Note that the conversion to the GDOS involves averaging over a certain q-range

5.2 Neutron backscattering spectroscopy

Neutron backscattering spectroscopy is a technique which allows to achieve very high energy resolution, in the μeV range. The backscattering technique is based on the fact that for Bragg angles close to 90°, the Bragg reflected wavelength band $\Delta\lambda$

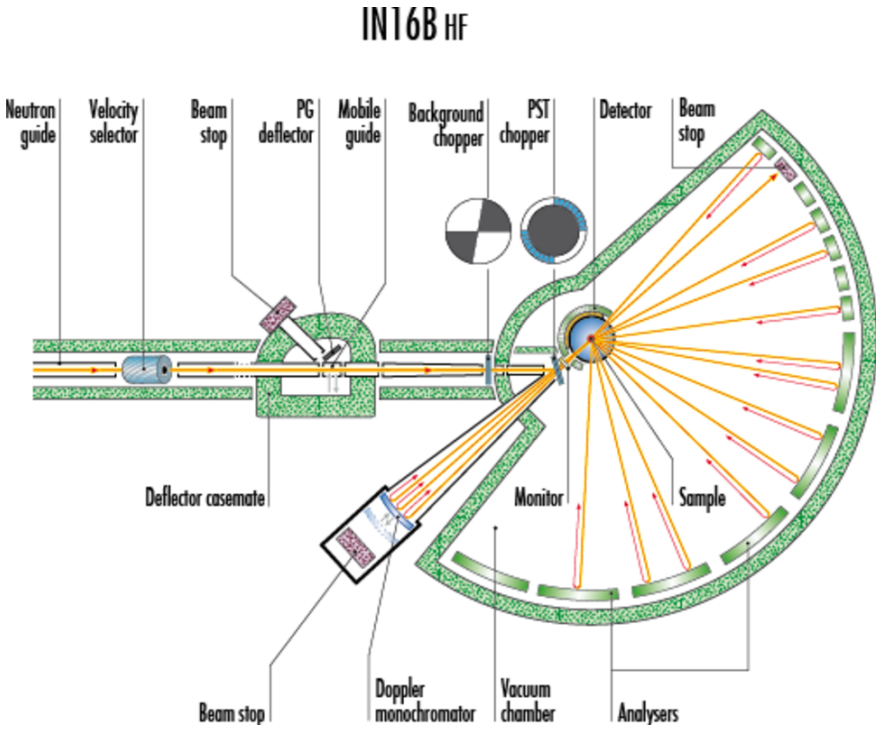

Figure 5.4: Schematic sketch of the IN16B backscattering spectrometer at the ILL, in its high flux configuration. The figure was taken from [112].

becomes very narrow. This can be seen by differentiating Bragg's law $\lambda = 2d \sin\theta$:

$$\frac{\Delta\lambda}{\lambda} = \frac{\Delta d}{d} + \cot\theta\,\Delta\theta, \tag{5.2}$$

where $\Delta\theta$ is the uncertainty in angle, *i.e.* the divergence of the beam. $\Delta d/d$ is the relative uncertainty in lattice spacing and can be interpreted as the relative width of the wavelength band for an infinitely sharp collimated beam, and is mainly related to the quality of the crystal. For $\theta = 90°$ the second term in Eq. (5.2) vanishes, meaning that $\Delta\lambda/\lambda$ is independent, to first order, of the divergence of the beam [113]. The backscattering technique thus uses a Bragg angle close to 90° for the selection and for the analysis of the energy of the neutrons, in order to achieve highest possible resolution [113].

An illustration of the neutron backscattering spectrometer IN16B at the ILL, which have been used in this thesis, is shown in Figure 5.4. The basic operation of this instrument will be described below. First, the neutron velocity band is se-

lected in a velocity selector. The background chopper pulses the beam, which is then deflected onto a Doppler monochromator. The Doppler monochromator consists of high quality silicon crystals mounted on a so-called Doppler drive, a device allowing the monochromator to move forwards and backwards. A 90° Bragg reflection from monochromator crystals selects neutrons with wavelength of 6.271 Å (for Si(111) crystals) [112, 114]. The selected neutron wavelength is allowed to vary by varying the speed of the Doppler drive, because the energy of the Bragg reflected neutrons depend on the relative speed of the neutrons and the Doppler drive. The Bragg scattered neutrons go back through slits in the rotating deflector, whilst the background chopper is closed during this time interval, allowing to significantly reduce the background. This leads to a pulsed beam of neutrons, with an energy band determined by the Doppler drive frequency, is incident on the sample. Neutrons are scattered from the sample, and only those with a certain final energy, determined by the backscattering reflection at the analyser crystals, are reflected to the detectors and counted [112, 114]. Thus, IN16b can be considered as an indirect geometry spectrometer where the final energy is determined by Bragg scattering of the analyzer crystal, whilst the incident energy is varied in a known way by the Doppler drive.

Depending on how the Doppler drive is setup, different measurement types are possible. If the Doppler drive frequency is set to zero, only the elastically scattered neutrons are reaching the detector. This mode can be used to measure the elastic intensity as a function of temperature, which can provide information about the mean squared displacement and qualitative information of relaxational dynamics in the sample (*i.e.* which temperature range the dynamics is accessible to the instrument timescales). If the Doppler drive is moved with a periodic velocity profile, an energy spectrum can be obtained. The maximum accessible energy transfer is typically in the range $10 - 100$ μeV, and is determined by the maximum velocity of the Doppler drive.

Chapter 6

Summary of results

6.1 Cation dynamics in the $MA_{1-x}FA_xPbI_3$ system

The results on the $MA_{1-x}FA_xPbI_3$ materials are reported in Papers I and II. Motivated by the lack of understanding pertaining to the structure of the low-temperature phase of $FAPbI_3$, and how the doping of MA allows to stabilize the perovskite structure of $FAPbI_3$, the local structure and vibrational dynamics in $MA_{1-x}FA_xPbI_3$ (x = 0.0, 0.6, 0.9, and 1.0) were investigated by INS combined with first-principles calculations. A particular focus was on probing the vibrational dynamics and local structure of the FA cation in the low-temperature disordered γ-phase, of which only limited information are, so far, available. The use of density functional theory (DFT) and *ab-initio* molecular dynamics simulations in combination with by the INS data, which is particularly sensitive to the organic cations, allowed to obtain a detailed atomistic understanding of the cation vibrations and underlying local structure around the organic cations in the materials. In particular, by analysis of the INS data in combination with the DFT calculations, a complete assignment of the full vibrational spectrum of $FAPbI_3$ was obtained. Further, the INS experiments on $FAPbI_3$ provide direct evidence of the formation of a low temperature orientational glass, thus confirming previous studies which have indicated this. The combination of the INS and first-principles allowed further to clarify some details about the stabilization of the perovskite structure of $FAPbI_3$ by doping with small amounts of MA organic cations. In particular, it was found that the hydrogen-bonding interactions around the formamidinium cations are strengthened as a result of cage deformation, and that this is accompanied by a weakening of the methylammonium interactions with the surrounding framework. One may hypothesize that these interactions involving the FA cations results in a locking effect, which strongly increases the stabilization

of the perovskite structure of $FAPbI_3$. In order to obtain further information of the dynamics of organic cations in $MA_{1-x}FA_xPbI_3$, the rotational dynamics of organic cations were also studied by using QENS. A particular focus of this study was to determine the details of the FA cation rotational dynamics across all crystallographic phases. The results show that, in the high-temperature cubic phase of $FAPbI_3$, the FA cations undergo nearly isotropic rotations with a relatively low activation energy of about 24 meV which is similar to the thermal energy at ambient temperature. In the tetragonal intermediate-temperature tetragonal phase, the FA cation performs reorientational motions between preferred orientations determined by the distortions from the cubic perovskite structure. However, in the low-temperature tetragonal phase of FAPI, the data indicates that the FA cation dynamics is much more complex, and most likely featured by a distribution of relaxation times and activation energies and related to the formation of an orientational glass of FA below 140 K. The analysis was extended to include methylammonium-doped solid solutions $MA_{1-x}FA_xPbI_3$. Interestingly, it was found found that the MA cation dynamics become drastically faster in the low-temperature phase of $MA_{0.4}FA_{0.6}PbI_3$ and that the organic cation dynamics is much less dependent on temperature in the mixed phases which is directly linked to the suppression of several structural phase transitions and an increasing disorder. This provides further support of the hypothesis from the INS results, that the strengthening of the $FA-PbI_3$ framework interactions upon doping with MA cations, introduces a locking effect, which strongly increases the stabilization of the perovskite structure. Such detailed understanding of how MA doping leads to a stabilization of the perovskite structure of $FAPbI_3$ is crucial for further development of new materials with higher stability. In particular, the main hindrance in using $FAPbI_3$ in a real photovoltaic device, is the poor stability of the perovskite phase, which rapidly transforms into a hexagonal polymorph, of little use to photovoltaics. Thus, the results presented in this work could thus lead to new design strategies for improving the stability of $FAPbI_3$, and other metal halide perovskites.

6.2 Hydride-ion dynamics in $SrVO_2H$

The results on the hydride-ion dynamics in $SrVO_2H$ is reported in Papers III and IV. The diffusional dynamics of hydride-ions in the layered perovskite-type oxyhydride $SrVO_2H$ was studied by QENS techniques. An exhaustive analysis of QENS data from both neutron time-of-flight and backscattering spectroscopy, allowing to probe a wide dynamic range, show that hydride-ions exhibit two-dimensional diffusion confined to the *ab*-crystallographic plane. This 2D diffusion mechanism could

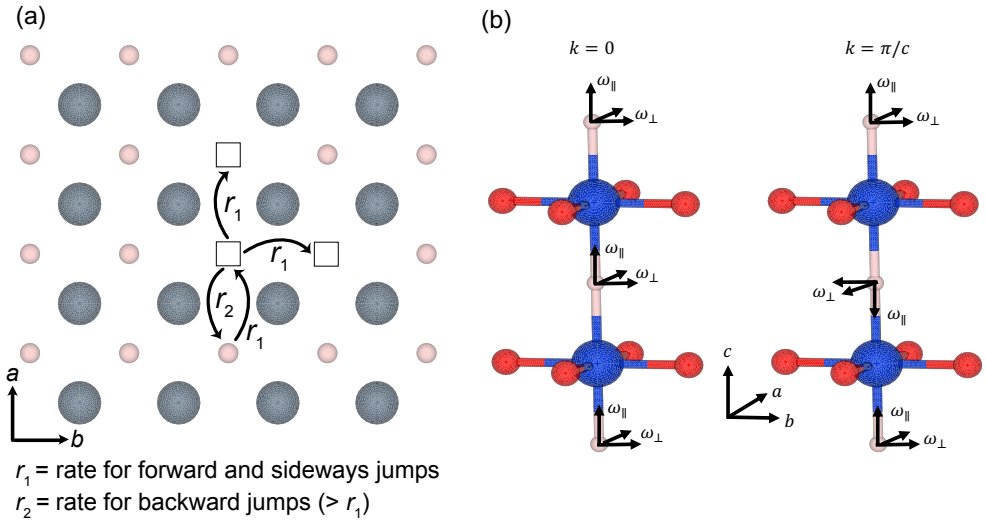

Figure 6.1: (a) Schematic sketch of the hydride-ion diffusion mechanism in the *ab*-plane of $SrVO_2H$, from Paper III, Ref. [90]. (b) Illustration of the vibrational modes of the hydride ions in $SrVO_2H$. The vibrational modes divide into a localized degenerate bending mode (labelled $\omega_\perp$) and a highly dispersed stretching mode (labelled $\omega_\parallel$). Both of these modes are split due to the AFM structure. Sr, V, O, and H atoms are illustrated as grey, blue, red, and pink spheres respectively.

be described as a temporally correlated vacancy assisted jump diffusion, with an increased rate for backward jumps. It should be stressed that such a correlated diffusion mechanism is usually not considered in QENS experiments on ionic conductors in general. The analysis methods applied in Paper III might thus be of more general use for interpreting QENS data of solid ionic conductors where the concentration of mobile species is high, that is, the vacancy concentration is low. A schematic sketch of the correlated hydride-ion diffusion mechanism in $SrVO_2H$ is shown in Figure 6.1 (a). These correlation effects occurs due to the small amount of hydride-ion vacancies present in the material. This means that once a hydride-ion has made a jump to a vacant site, the probability of a return jump is significantly enhanced because there is a larger (than average) probability to find a vacancy at the original position. Such a correlated diffusion mechanism is expected to decrease the hydride-ion conductivity because a large portion of the hydride-ion dynamics becomes temporally localized around a particular vacancy. These results thus suggests that tuning of the hydride-ion and/or oxygen-ion vacancy concentration in $SrVO_2H$ thus repre-

sents a promising gateway for improving the ionic conductivity of this already highly hydride-ion conducting material. In order to gain more insight of the vanadium-hydrogen bonding situation in $SrVO_2H$, and to understand how this is related to the hydride-ion diffusion, the vibrational dynamics of $SrVO_2H$ was studied by INS and infrared spectroscopy in combination with phonon calculations based on density functional theory. The vibrational modes of the hydride ions was found to divide into a degenerate bending mode (perpendicular the H−V−H chain direction) and a highly dispersed stretching mode (along the H−V−H chain direction), see Figure 6.1 (b). The bending mode, which is seen at around 800 cm^{-1}, was found to be clearly split into two components separated by about 50 cm^{-1}, and this splitting was shown to occur due to the doubling of the unit cell from the antiferromagnetic structure. Interestingly, analysis of the results from the DFT calculated phonon dispersion in combination with the INS data, reveal unusually large spin-phonon coupling effects, that stiffens H-based modes by 50−100 cm^{-1}, even though super-exchange coupling via H is relatively small. Large frequency shifts (on the same order of magnitude) was also found for the V−O modes. These results provide direct evidence for the novel and interesting many-body effects that can occur in strontium vanadium oxyhydride phases, where interesting couplings between the magnetism and hydrogen dynamics can occur.

Chapter 7

Conclusions and outlook

To conclude, this thesis has presented neutron scattering investigations on the dynamical properties of two interesting classes of materials, namely the organometal halide perovskite system $MA_{1-x}FA_xPbI_3$, and the transition metal oxyhydride $SrVO_2H$.

For the $MA_{1-x}FA_xPbI_3$ system, the results have provided an detailed analysis of the FA organic cation dynamics. Both the vibrational and rotational dynamics of the FA cation have been characterized by using inelastic and quasielastic neutron scattering, respectively. Such a detailed knowledge of the FA organic cation dynamics, have allowed to increase the fundamental understanding of the metal halide perovskites materials, in general, and in particular with regards to FA-containing materials, which nowadays are gaining an increasing interest. These new insights are hoped to be used for a rational design of new materials with, hopefully, unprecedented properties. Given the large chemical space to explore for the development of new compounds, it is critical to increase the fundamental understanding of these materials, of which the research presented in this thesis represents a small part.

Of course, there is a lot of future work to build on to the results presented in this thesis, some which I have already initiated. In particular, in Paper II, it was found that the $MA_{1-x}FA_xPbI_3$ materials are featured by a highly overdamped phonon dynamics in the intermediate and high temperature phases. While this observed "phonon melting" happens at the onset temperature for the dynamics of the organic cation (MA), recent studies on the very similar (all-inorganic) material $CsPbBr_3$ suggests that the observed "phonon melting" is a generic feature of the soft lead iodide framework [16, 18]. Accordingly, the nature and effect of the organic cation and perovskite lattice dynamics on the structural and optical properties of MHPs remains unclear. To answer this question, I thus plan to conduct an variable temperature INS study (beamtime is planned for later in this year) on the all-inorganic perovskite

$CsPbI_3$, probing the phonon density of states in all crystallographic phases. Through a comparison with the $MA_{1-x}FA_xPbI_3$ system, which have been studied in this thesis, this is hoped to elucidate even further the "phonon melting" phenomena in lead iodide perovskites, and would significantly advance the fundamental understanding of the metal halide perovskites in general.

Another future project which is related to the $MA_{1-x}FA_xPbI_3$ samples, concerns trying to investigate the MA dynamics in thin films of $MAPbI_3$ by using neutron scattering. INS studies of thin film samples are generally a large technical challenge due to the drastically reduced sample volume. This project builds onto the results in Paper V (which is listed as an additional publication not included in the thesis), and the plan for this project is to use a method developed recently by Wolff *et al.* [115], in which the neutron wave field can be enhanced in a sample with a quantum well resonator structure. Specifically, by using a multi-layer structure where a sample material is sandwiched between two layers with high scattering length density, a quantum well is formed for the neutrons. An example of this is shown in Figure 7.1 which shows a sketch of a possible quantum well resonator sample made from $MAPbI_3$. The sample of $MAPbI_3$ is sandwiched between layers of Ni, which has a higher scattering length density, thus allowing a potential well to be formed. When shined at grazing incidence (below the critical angle of total reflection), at critical angles where the wavevector transfer matches the resonance condition of the potential well, a standing wave is formed with an increased amplitude of the neutron wave function, resulting in an increased probability of incoherent scattering from the sample [115]. In a first step, the plan is to grow such a sample, with $MAPbI_3$ sandwiched between layers of high scattering length density. The plan is then to first measure the neutron reflectometry, in order to evaluate if such a sample could work as a quantum resonator. If successful, the second step would then be to try to measure the inelastic and/or quasielastic neutron scattering from the film.

Another project which already has been initiated concerns so-called "2D" lead iodide perovskites. These materials are formed by having a larger organic cation on the A-site in the perovskite, too large to fit into the perovskite cage. This disrupts the perovskite framework, leading to a layered structure consisting of (one or several) inorganic sheets of PbI_6 octahedra separated by layers of organic cations, held together by electrostatic forces. Since the organic cations are electronically insulating, electron and hole transport is hindered between different layers, thus rendering the materials as quasi-2D [116]. Such materials are currently attracting an increasing interest because they show higher stability towards moisture, thus opening new paths for stabilizing perovskite-based photovoltaic devices [116]. However, little is known of the dynamical properties (organic cation and lattice dynamics) in these

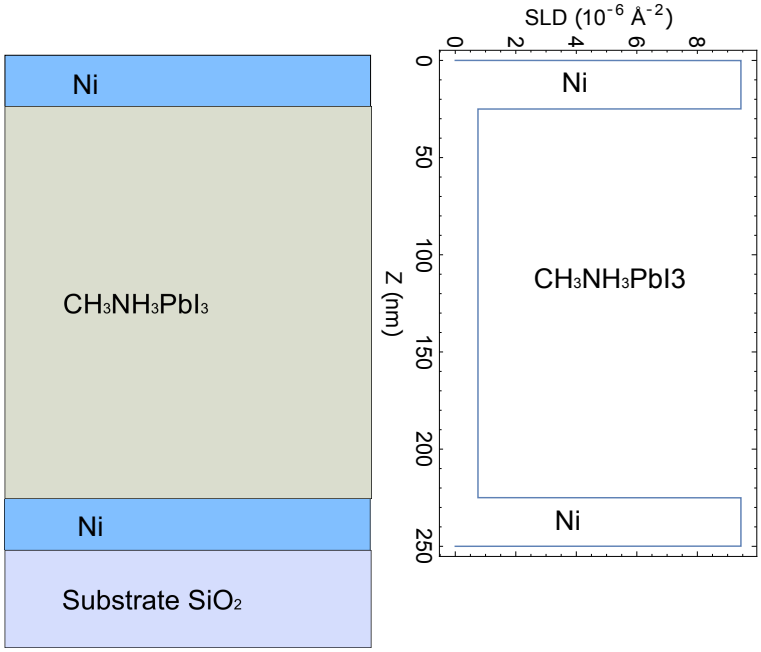

Figure 7.1: Schematic sketch of a possible quantum well resonator sample made from $MAPbI_3$ ($CH_3NH_3PbI_3$. The sample of $MAPbI_3$ is sandwiched between layers of Ni, which has a relatively high scattering length density.

materials, and as for their 3D counterparts, the dynamics is believed to play a large role in the materials properties [117]. I have already performed INS and QENS measurements on the two prototypical 2D lead iodide perovskites BA_2PbI_4 (BA = butylammonium;) and PEA_2PbI_4 (PEA = phenylethylammonium). The aim of this project is to characterize both the reorientational organic cation dynamics and the lattice dynamics in these two prototypical materials.

With regards to the oxyhydride $SrVO_2H$, this thesis present detailed investigations of the hydride-ion dynamics in $SrVO_2H$. By combining neutron backscattering and time-of-flight spectroscopy, allowing to probe a wide range of timescales, the hydride-ion diffusion mechanism have been characterized in detail (Paper III). Interestingly this study shows that the hydride-ion diffusion in $SrVO_2H$ is confined to the *ab*-crystallographic plane (*i.e.* 2D diffusion), and that the diffusion step is temporally correlated, with an increased rate for backward jumps. A new perspective to advance further the understanding of hydride-ion diffusion in $SrVO_2H$ has been recently given by preliminary data from our collaborators at Stockholm University,

which showed that $SrVO_2H$ can form non-reversibly a cubic anion-disordered phase by heating in a strictly oxygen-free environment. In such a cubic phase, the hydride and oxygen anions are disordered, and one thus expects 3D diffusion. This presumably leads to a drastically different diffusion process and one can hypothesize that the correlations effects observed in the hydride-ion diffusion in the *ab*-plane of $SrVO_2H$ are reduced in the cubic phase, which possibly could lead to an increased hydride-ion mobility. An upcoming future study is thus to study this cubic phase $SrVO_2H$, first by neutron diffraction, in order to elucidate the nature of the phase transition (both structural and possible magnetic), and later on with QENS and INS in order to study the hydride-ion diffusion and vibrational dynamics.

With regards to the INS study of $SrVO_2H$ (Paper IV), it was found rather surprisingly, that $SrVO_2H$ shows a large spin-phonon coupling, leading to large energy shifts and splittings of the H based vibrations. Such large spin-phonon coupling is rare and illustrate the interesting many-body effects that can occur in strontium vanadium oxyhydride phases. However, the magnetic ordering of $SrVO_2H$ is found to be intact far above room temperature [89, 90] and its possible that the Néel temperature is close to or even above the decomposition temperature of the material. In effect, it was impossible to study the paramagnetic phase of the material in this study. Still, in order to prove the strong spin-phonon coupling experimentally, one would need to measure the INS spectra as a function of temperature upon heating through the Néel temperature. In a future study, I plan to investigate the vibrational dynamics in the two related Ruddlesden-Popper strontium vanadium oxyhydride phases $Sr_{n+1}V_nO_{2n+1}H_n$ ($n = 1, 2$) [89]. In particular, $Sr_{n+1}V_nO_{2n+1}H_n$ has a lower Néel temperature than $SrVO_2H$ (170 K and 240 K for $n = 1$ and 2, respectively [89]) allowing to measure the INS spectrum directly in both the magnetically ordered and paramagnetic phases, which could allow to directly observe possible effects of spin-phonon coupling.

Acknowledgements

I would like to thank my main supervisor Maths Karlsson for all support, quick feedback, for sharing knowledge on how to conduct good research, and for giving me the opportunity to do my PhD at Chalmers. I also like to thank my examiner Lars-Gunnar Johansson and my assistant supervisor Max Wolff. Thanks also to my past and present colleagues and office friends Yuan-Chih, Mikael, Elena, Reddy, Laura, and Carin, and all other colleagues at the OOMK division. I would like to thank Ulrich Häussermann for great scientific inputs/discussions and for synthesizing samples. Lorenzo Malavasi for providing interesting samples. I further like to thank all the scientists at the neutron facilities I have visited, especially Adrien Perrichon, Michael Koza, Franz Demmel, Jeff Armstrong, and Masato Matsuura, for great help with the experiments and data analysis, and for making the beamtimes interesting and fun. Lastly, I also like to express my greatest appreciation of my family for all the support. Especially to Petra, my life partner, thanks for your enormous support and for keeping up with me.

Bibliography

[1] B. Lojek, *History of Semiconductor Engineering* (Springer Verlag, 2007).

[2] National Renewable Energy Laboratory, Best Research-Cell Efficiency Chart, https://www.nrel.gov/pv/cell-efficiency.html, accessed: 2021-05-24.

[3] N. J. Jeon, J. H. Noh, W. S. Yang, Y. C. Kim, S. Ryu, J. Seo, and S. I. Seok, Nature **517**, 476 (2015).

[4] D. Weber, Zeitschrift für Naturforschung B **33**, 1443 (1978).

[5] A. Poglitsch and D. Weber, The Journal of Chemical Physics **87**, 6373 (1987).

[6] A. Kojima, K. Teshima, Y. Shirai, and T. Miyasaka, Journal of the American Chemical Society **131**, 6050 (2009).

[7] M. M. Lee, J. Teuscher, T. Miyasaka, T. N. Murakami, and H. J. Snaith, Science **338**, 643 (2012).

[8] D. A. Egger, A. Bera, D. Cahen, G. Hodes, T. Kirchartz, L. Kronik, R. Lovrincic, A. M. Rappe, D. R. Reichman, and O. Yaffe, Advanced Materials **30**, 1800691 (2018).

[9] T. Ihn, *Semiconductor Nanostructures: Quantum States and Electronic Transport* (OUP Oxford, 2010).

[10] Z. Li, T. R. Klein, D. H. Kim, M. Yang, J. J. Berry, M. F. A. M. van Hest, and K. Zhu, Nature Reviews Materials **3**, 18017 (2018).

[11] S. D. Stranks, G. E. Eperon, G. Grancini, C. Menelaou, M. J. P. Alcocer, T. Leijtens, L. M. Herz, A. Petrozza, and H. J. Snaith, Science **342**, 341 (2013).

[12] J. Berry, T. Buonassisi, D. A. Egger, G. Hodes, L. Kronik, Y.-L. Loo, I. Lubomirsky, S. R. Marder, Y. Mastai, J. S. Miller, D. B. Mitzi, Y. Paz, A. M. Rappe, I. Riess, B. Rybtchinski, O. Stafsudd, V. Stevanovic, M. F. Toney, D. Zitoun, A. Kahn, D. Ginley, and D. Cahen, Advanced Materials **27**, 5102 (2015).

[13] N. P. Gallop, O. Selig, G. Giubertoni, H. J. Bakker, Y. L. Rezus, J. M. Frost, T. L. Jansen, R. Lovrincic, and A. A. Bakulin, J. Phys. Chem. Lett. **9**, 5987 (2018).

[14] T. Chen, B. J. Foley, B. Ipek, M. Tyagi, J. R. D. Copley, C. M. Brown, J. J. Choi, and S.-H. Lee, Phys. Chem. Chem. Phys. **17**, 31278 (2015).

[15] F. Wang, Y. Fu, M. E. Ziffer, Y. Dai, S. F. Maehrlein, and X.-Y. Zhu, Journal of the American Chemical Society **143**, 5 (2021).

[16] T. Lanigan-Atkins, X. He, M. J. Krogstad, D. M. Pajerowski, D. L. Abernathy, G. N. M. N. Xu, Z. Xu, D. Y. Chung, M. G. Kanatzidis, S. Rosenkranz, R. Osborn, and O. Delaire, Nature Materials 10.1038/s41563-021-00947-y (2021).

[17] D. Zhang, X. Hu, T. Chen, D. L. Abernathy, R. Kajimoto, M. Nakamura, M. Kofu, B. J. Foley, M. Yoon, J. J. Choi, and S.-H. Lee, Phys. Rev. B **102**, 224310 (2020).

[18] O. Yaffe, Y. Guo, L. Z. Tan, D. A. Egger, T. Hull, C. C. Stoumpos, F. Zheng, T. F. Heinz, L. Kronik, M. G. Kanatzidis, J. S. Owen, A. M. Rappe, M. A. Pimenta, and L. E. Brus, Phys. Rev. Lett. **118**, 1 (2017).

[19] X. Y. Zhu and V. Podzorov, J. Phys. Chem. Lett. **6**, 4758 (2015).

[20] H. Zhu, K. Miyata, Y. Fu, J. Wang, P. P. Joshi, D. Niesner, K. W. Williams, S. Jin, and X.-Y. Zhu, Science **353**, 1409 (2016).

[21] K. Miyata, T. L. Atallah, and X. Y. Zhu, Sci. Adv. **3**, 1 (2017).

[22] K. Momma and F. Izumi, J. Appl. Crystallogr. **44**, 1272 (2011).

[23] M. A. Hayward, E. J. Cussen, J. B. Claridge, M. Bieringer, M. J. Rosseinsky, C. J. Kiely, S. J. Blundell, I. M. Marshall, and F. L. Pratt, Science **295**, 1882 (2002).

[24] J. B. Goodenough, Chemistry of Materials **26**, 820 (2014).

[25] Y. Wei, H. Gui, X. Li, Z. Zhao, Y. H. Zhao, and W. Xie, J. Phys. Condens. Matter **27**, 10.1088/0953-8984/27/20/206001 (2015).

[26] K. Liu, Y. Hou, X. Gong, and H. Xiang, Sci. Rep. **6**, 1 (2016).

[27] Y. Kobayashi, Y. Tang, T. Kageyama, H. Yamashita, N. Masuda, S. Hosokawa, and H. Kageyama, Journal of the American Chemical Society **139**, 18240 (2017).

[28] T. Yamamoto, D. Zeng, T. Kawakami, V. Arcisauskaite, K. Yata, M. A. Patino, N. Izumo, J. E. McGrady, H. Kageyama, and M. A. Hayward, Nat. Commun. **8**, 10.1038/s41467-017-01301-0 (2017).

[29] Y. Kobayashi, O. Hernandez, C. Tassel, and H. Kageyama, Sci. Technol. Adv. Mater. **18**, 905 (2017).

[30] T. Yajima, A. Kitada, Y. Kobayashi, T. Sakaguchi, G. Bouilly, S. Kasahara, T. Terashima, M. Takano, and H. Kageyama, J. Am. Chem. Soc. **134**, 8782 (2012).

[31] C. A. Bridges, F. Fernandez-Alonso, J. P. Goff, and M. J. Rosseinsky, Adv. Mater. **18**, 3304 (2006).

[32] Y. Kobayashi, O. J. Hernandez, T. Sakaguchi, T. Yajima, T. Roisnel, Y. Tsujimoto, M. Morita, Y. Noda, Y. Mogami, A. Kitada, M. Ohkura, S. Hosokawa, Z. Li, K. Hayashi, Y. Kusano, J. E. Kim, N. Tsuji, A. Fujiwara, Y. Matsushita, K. Yoshimura, K. Takegoshi, M. Inoue, M. Takano, and H. Kageyama, Nat. Mater. **11**, 507 (2012).

[33] N. Masuda, Y. Kobayashi, O. Hernandez, T. Bataille, S. Paofai, H. Suzuki, C. Ritter, N. Ichijo, Y. Noda, K. Takegoshi, C. Tassel, T. Yamamoto, and H. Kageyama, J. Am. Chem. Soc. **137**, 15315 (2015).

[34] T. Yajima, F. Takeiri, K. Aidzu, H. Akamatsu, K. Fujita, W. Yoshimune, M. Ohkura, S. Lei, V. Gopalan, K. Tanaka, C. M. Brown, M. A. Green, T. Yamamoto, Y. Kobayashi, and H. Kageyama, Nature Chemistry **7**, 1017 (2015).

[35] G. Kobayashi, Y. Hinuma, S. Matsuoka, A. Watanabe, M. Iqbal, M. Hirayama, M. Yonemura, T. Kamiyama, I. Tanaka, and R. Kanno, Science **351**, 1314 (2016).

[36] J. P. Correa-Baena, A. Abate, M. Saliba, W. Tress, T. Jesper Jacobsson, M. Grätzel, and A. Hagfeldt, Energy Environ. Sci. **10**, 710 (2017).

[37] W. S. Yang, N. J. J. Jun Hong Noh, Y. C. Kim, S. Ryu, J. Seo, and S. I. Seok, Science **348**, 2013 (2015).

[38] K. Drużbicki, R. Lavén, J. Armstrong, L. Malavasi, F. Fernandez-Alonso, and M. Karlsson, J. Phys. Chem. Lett. **12**, 3503 (2021).

[39] T. Baikie, Y. Fang, J. M. Kadro, M. Schreyer, F. Wei, S. G. Mhaisalkar, M. Graetzel, and T. J. White, J. Mater. Chem. A **1**, 5628 (2013).

[40] M. T. Weller, O. J. Weber, P. F. Henry, A. M. Di Pumpo, and T. C. Hansen, Chem. Commun. **51**, 4180 (2015).

[41] K. Druzbicki, R. S. Pinna, S. Rudić, M. Jura, G. Gorini, and F. Fernandez-Alonso, J. Phys. Chem. Lett. **7**, 4701 (2016).

[42] Y. Rakita, O. Bar-Elli, E. Meirzadeh, H. Kaslasi, Y. Peleg, G. Hodes, I. Lubomirsky, D. Oron, D. Ehre, and D. Cahen, Proceedings of the National Academy of Sciences **114**, E5504 (2017).

[43] J. Breternitz, F. Lehmann, S. A. Barnett, H. Nowell, and S. Schorr, Angewandte Chemie International Edition **59**, 424 (2020).

[44] A. N. Beecher, O. E. Semonin, J. M. Skelton, J. M. Frost, M. W. Terban, H. Zhai, A. Alatas, J. S. Owen, A. Walsh, and S. J. L. Billinge, ACS Energy Letters **1**, 880 (2016).

[45] N. J. Weadock, P. M. Gehring, A. Gold-Parker, I. C. Smith, H. I. Karunadasa, and M. F. Toney, Phys. Rev. Lett. **125**, 075701 (2020).

[46] O. J. Weber, D. Ghosh, S. Gaines, P. F. Henry, A. B. Walker, M. S. Islam, and M. T. Weller, Chem. Mater. **30**, 3768 (2018).

[47] A. Pisanu, C. Ferrara, P. Quadrelli, G. Guizzetti, M. Patrini, C. Milanese, C. Tealdi, and L. Malavasi, J. Phys. Chem. C **121**, 8746 (2017).

[48] C. C. Stoumpos, C. D. Malliakas, and M. G. Kanatzidis, Inorg. Chem. **52**, 9019 (2013).

[49] Q. Han, S. H. Bae, P. Sun, Y. T. Hsieh, Y. Yang, Y. S. Rim, H. Zhao, Q. Chen, W. Shi, G. Li, and Y. Yeng, Adv. Mater. **28**, 2253 (2016).

[50] J. J. Choi, L. W. Harriger, J. Ruff, T. Chen, J. Lee, C. Park, C. M. Brown, B. J. Foley, M. Yoon, and S.-H. Lee, Sci. Adv. **2**, e1601650 (2016).

[51] D. H. Fabini, C. C. Stoumpos, G. Laurita, A. Kaltzoglou, A. G. Kontos, P. Falaras, M. G. Kanatzidis, and R. Seshadri, Angew. Chemie - Int. Ed. **55**, 15392 (2016).

[52] T. Chen, W. L. Chen, B. J. Foley, J. Lee, J. P. Ruff, J. Y. Ko, C. M. Brown, L. W. Harriger, D. Zhang, C. Park, M. Yoon, Y. M. Chang, J. J. Choi, and S. H. Lee, Proc. Natl. Acad. Sci. U. S. A. **114**, 7519 (2017).

[53] S. Sun, Z. Deng, Y. Wu, F. Wei, F. Halis Isikgor, F. Brivio, M. W. Gaultois, J. Ouyang, P. D. Bristowe, A. K. Cheetham, and G. Kieslich, Chem. Commun. **53**, 7537 (2017).

[54] D. H. Fabini, T. Hogan, H. A. Evans, C. C. Stoumpos, M. G. Kanatzidis, and R. Seshadri, J. Phys. Chem. Lett. **7**, 376 (2016).

[55] D. H. Fabini, T. A. Siaw, C. C. Stoumpos, G. Laurita, D. Olds, K. Page, J. G. Hu, M. G. Kanatzidis, S. Han, and R. Seshadri, J. Am. Chem. Soc. **139**, 16875 (2017).

[56] O. J. Weber, B. Charles, and M. T. Weller, J. Mater. Chem. A **4**, 15375 (2016).

[57] J. W. Lee, D. J. Seol, A. N. Cho, and N. G. Park, Adv. Mater. **26**, 4991 (2014).

[58] T. Jesper Jacobsson, J. P. Correa-Baena, M. Pazoki, M. Saliba, K. Schenk, M. Grätzel, and A. Hagfeldt, Energy Environ. Sci. **9**, 1706 (2016).

[59] A. Francisco-López, B. Charles, M. I. Alonso, M. Garriga, M. Campoy-Quiles, M. T. Weller, and A. R. Goñi, J. Phys. Chem. C **124**, 3448 (2020).

[60] A. M. Leguy, J. M. Frost, A. P. McMahon, V. G. Sakai, W. Kochelmann, C. Law, X. Li, F. Foglia, A. Walsh, B. C. O'Regan, J. Nelson, J. T. Cabral, and P. R. Barnes, Nat. Commun. **6**, 10.1038/ncomms8124 (2015).

[61] B. Li, Y. Kawakita, Y. Liu, M. Wang, M. Matsuura, K. Shibata, S. Ohira-Kawamura, T. Yamada, S. Lin, K. Nakajima, and S. F. Liu, Nature Communications **8**, 16086 (2017).

[62] D. J. Kubicki, D. Prochowicz, A. Hofstetter, P. Péchy, S. M. Zakeeruddin, M. Grätzel, and L. Emsley, J. Am. Chem. Soc. **139**, 10055 (2017).

[63] V. C. A. Taylor, D. Tiwari, M. Duchi, P. M. Donaldson, I. P. Clark, D. J. Fermin, and T. A. A. Oliver, J. Phys. Chem. Lett. **9**, 895 (2018).

[64] A. Mattoni, A. Filippetti, M. I. Saba, and P. Delugas, J. Phys. Chem. C **119**, 17421 (2015).

[65] J. Li, M. Bouchard, P. Reiss, D. Aldakov, S. Pouget, R. Demadrille, C. Aumaitre, B. Frick, D. Djurado, M. Rossi, and P. Rinke, J. Phys. Chem. Lett. **9**, 3969 (2018).

[66] I. P. Swainson, C. Stock, S. F. Parker, L. Van Eijck, M. Russina, and J. W. Taylor, Phys. Rev. B - Condens. Matter Mater. Phys. **92**, 2 (2015).

[67] A. A. Bakulin, O. Selig, H. J. Bakker, Y. L. Rezus, C. Müller, T. Glaser, R. Lovrincic, Z. Sun, Z. Chen, A. Walsh, J. M. Frost, and T. L. Jansen, J. Phys. Chem. Lett. **6**, 3663 (2015).

[68] E. M. Mozur, A. E. Maughan, Y. Cheng, A. Huq, N. Jalarvo, L. L. Daemen, and J. R. Neilson, Chem. Mater. **29**, 10168 (2017).

[69] G. M. Bernard, R. E. Wasylishen, C. I. Ratcliffe, V. Terskikh, Q. Wu, J. M. Buriak, and T. Hauger, J. Phys. Chem. A **122**, 1560 (2018).

[70] A. Johnston, G. Walters, M. I. Saidaminov, Z. Huang, K. Bertens, N. Jalarvo, and E. H. Sargent, ACS Nano **14**, 15107 (2020).

[71] K. T. Munson, J. R. Swartzfager, J. Gan, and J. B. Asbury, J. Phys. Chem. Lett. **11**, 3166 (2020).

[72] K. T. Munson and J. B. Asbury, J. Phys. Chem. C **125**, 5427 (2021).

[73] Z. Guo, Y. Wan, M. Yang, J. Snaider, K. Zhu, and L. Huang, Science **356**, 59 (2017).

[74] J. Ma and L. W. Wang, Nano Lett. **15**, 248 (2015).

[75] C. Quarti, E. Mosconi, and F. De Angelis, Phys. Chem. Chem. Phys. **17**, 9394 (2015).

[76] K. L. Brown, S. F. Parker, I. R. García, S. Mukhopadhyay, V. G. Sakai, and C. Stock, Phys. Rev. B **96**, 1 (2017).

[77] G. Schuck, F. Lehmann, J. Ollivier, H. Mutka, and S. Schorr, J. Phys. Chem. C **123**, 11436 (2019).

[78] M. Songvilay, Z. Wang, V. G. Sakai, T. Guidi, M. Bari, Z.-G. Ye, G. Xu, K. L. Brown, P. M. Gehring, and C. Stock, Phys. Rev. Materials **3**, 125406 (2019).

[79] V. K. Sharma, R. Mukhopadhyay, A. Mohanty, M. Tyagi, J. P. Embs, and D. D. Sarma, J. Phys. Chem. Lett. **11**, 9669 (2020).

[80] E. M. Mozur, J. C. Trowbridge, A. E. Maughan, M. J. Gorman, C. M. Brown, T. R. Prisk, and J. R. Neilson, ACS Materials Letters **1**, 260 (2019).

[81] E. M. Mozur, M. A. Hope, J. C. Trowbridge, D. M. Halat, L. L. Daemen, A. E. Maughan, T. R. Prisk, C. P. Grey, and J. R. Neilson, Chem. Mater. **32**, 6266 (2020).

[82] V. C. A. Taylor, D. Tiwari, M. Duchi, P. M. Donaldson, I. P. Clark, D. J. Fermin, and T. A. A. Oliver, J. Phys. Chem. Lett. **9**, 895 (2018).

[83] G. Fisicaro, A. La Magna, A. Alberti, E. Smecca, G. Mannino, and I. Deretzis, J. Phys. Chem. Lett. **11**, 1068 (2020).

[84] C. A. Bridges, G. R. Darling, M. A. Hayward, and M. J. Rosseinsky, Journal of the American Chemical Society **127**, 5996 (2005).

[85] T. Yamamoto and H. Kageyama, Chemistry Letters **42**, 946 (2013).

[86] H. Kageyama, T. Yajima, Y. Tsujimoto, T. Yamamoto, C. Tassel, and Y. Kobayashi, Bulletin of the Chemical Society of Japan **92**, 1349 (2019).

[87] T. Sakaguchi, Y. Kobayashi, T. Yajima, M. Ohkura, C. Tassel, F. Takeiri, S. Mitsuoka, H. Ohkubo, T. Yamamoto, J. e. Kim, N. Tsuji, A. Fujihara, Y. Matsushita, J. Hester, M. Avdeev, K. Ohoyama, and H. Kageyama, Inorganic Chemistry **51**, 11371 (2012).

[88] C. Tassel, Y. Goto, Y. Kuno, J. Hester, M. Green, Y. Kobayashi, and H. Kageyama, Angew. Chemie - Int. Ed. **53**, 10377 (2014).

[89] F. Denis Romero, A. Leach, J. S. Möller, F. Foronda, S. J. Blundell, and M. A. Hayward, Angew. Chemie - Int. Ed. **53**, 7556 (2014).

[90] R. Lavén, U. Häussermann, A. Perrichon, M. S. Andersson, M. S. Targama, F. Demmel, and M. Karlsson, Chemistry of Materials **33**, 2967 (2021).

[91] L. Jin, M. Lane, D. Zeng, F. K. Kirschner, F. Lang, P. Manuel, S. J. Blundell, J. E. McGrady, and M. A. Hayward, Angew. Chemie - Int. Ed. **57**, 5025 (2018).

[92] L. Jin and M. A. Hayward, Chem. Commun. **55**, 4861 (2019).

[93] C. Tassel, Y. Goto, D. Watabe, Y. Tang, H. Lu, Y. Kuno, F. Takeiri, T. Yamamoto, C. M. Brown, J. Hester, Y. Kobayashi, and H. Kageyama, Angewandte Chemie International Edition **55**, 9667 (2016).

[94] J. Zhang, G. Gou, and B. Pan, J. Phys. Chem. C **118**, 17254 (2014).

[95] Y. Tang, Y. Kobayashi, K. Shitara, A. Konishi, A. Kuwabara, T. Nakashima, C. Tassel, T. Yamamoto, and H. Kageyama, Chem. Mater. **29**, 8187 (2017).

[96] X. Liu, T. S. Bjørheim, and R. Haugsrud, J. Mater. Chem. A **5**, 1050 (2017).

[97] C. Eklöf-Österberg, R. Nedumkandathil, U. Häussermann, A. Jaworski, A. J. Pell, M. Tyagi, N. H. Jalarvo, B. Frick, A. Faraone, and M. Karlsson, J. Phys. Chem. C **123**, 2019 (2019).

[98] X. Liu, T. S. Bjørheim, L. Vines, Ø. S. Fjellvåg, C. Granerød, Ø. Prytz, T. Yamamoto, H. Kageyama, T. Norby, and R. Haugsrud, Journal of the American Chemical Society **141**, 4653 (2019).

[99] S. Yamaguchi, Science **351**, 1262 (2016).

[100] G. L. Squires, *Introduction to the Theory of Thermal Neutron Scattering* (Cambridge University Press, 1978).

[101] S. W. Lovesey, *Theory of Neutron Scattering from Condensed Matter Vol. I.* (Clarendon Press, 1984).

[102] R. Hempelmann, *Quasielastic Neutron Scattering and Solid State Diffusion* (Oxford University Press, 2000).

[103] F. Demmel, Quasielastic neutron scattering, https://www.isis.stfc.ac.uk/Pages/quasi-elastic-neutron-scattering13583.pdf (2013), accessed: 2021-05-23.

[104] L. Van Hove, Phys. Rev. **95**, 249 (1954).

[105] P. H. Mitchell, S. F. Parker, and A. J. Ramirez-Cuezta, *Vibrational Spectroscopy with Neutrons* (Word Scientific, 2005).

[106] A. Furrer, J. Mesot, and T. Strässle, *Neutron Scattering in Condensed Matter Physics* (World Scientific, 2009).

[107] B. Chazallon, H. Itoh, M. Koza, W. F. Kuhs, and H. Schober, Phys. Chem. Chem. Phys. **4**, 4809 (2002).

[108] M. Bée, *Quasielastic Neutron Scattering: Principles and Applications in Solid State Chemistry and Materials Science* (Adam Hilger, 1988).

[109] C. T. Chudley and R. J. Elliot, Proc. Phys. Soc. **77**, 353 (1961).

[110] IN5, Institut Laue Langevin, https://www.ill.eu/users/instruments/instruments-list/in5/description/instrument-layout, accessed: 2021-05-07.

[111] D. Richard, M. Ferrand, and G. J. Kearley, J. Neutron Res. **4**, 33 (1996).

[112] IN16B, Institut Laue Langevin, https://www.ill.eu/users/instruments/instruments-list/in16b/description/instrument-layout, accessed: 2021-05-21.

[113] Web site for neutron backscattering spectroscopy, https://ah-backscattering.pagesperso-orange.fr, accessed: 2021-05-22.

[114] B. Frick, E. Mamontov, L. van Eijck, and T. Seydel, Z. Phys. Chem. **224**, 33 (2010).

[115] M. Wolff, A. Devishvili, J. A. Dura, F. A. Adlmann, B. Kitchen, G. K. Pálsson, H. Palonen, B. B. Maranville, C. F. Majkrzak, and B. P. Toperverg, Phys. Rev. Lett. **123**, 016101 (2019).

[116] G. Grancini and M. K. Nazeeruddin, Nature Reviews Materials **4**, 4 (2019).

[117] X. Hu, D. Zhang, T. Chen, A. Z. Chen, E. N. Holmgren, Q. Zhang, D. M. Pajerowski, M. Yoon, G. Xu, J. J. Choi, and S.-H. Lee, The Journal of Chemical Physics **152**, 014703 (2020).